

## Is there any linkage between interstellar aldehyde and alcohol?

SUMAN KUMAR MONDAL,<sup>1</sup> PRASANTA GORAI,<sup>2,1</sup> MILAN SIL,<sup>1</sup> RANA GHOSH,<sup>1</sup> EMMANUEL E. ETIM,<sup>3</sup> SANDIP K CHAKRABARTI,<sup>1</sup> TAKASHI SHIMONISHI,<sup>4,5</sup>  
NAOKI NAKATANI,<sup>6</sup> KENJI FURUYA,<sup>7</sup> JONATHAN C. TAN,<sup>2,8</sup> AND ANKAN DAS<sup>1</sup>

<sup>1</sup>Indian Centre for Space Physics, 43 Chalantika, Garia Station Road, Kolkata 700084, India

<sup>2</sup>Department of Space, Earth & Environment, Chalmers University of Technology, SE-412 96 Gothenburg, Sweden

<sup>3</sup>Department of Chemical Sciences, Federal University Wukari, Katsina-Ala Road, P.M.B. 1020 Wukari, Taraba State, Nigeria

<sup>4</sup>Center for Transdisciplinary Research, Niigata University, Nishi-ku, Niigata 950-2181, Japan

<sup>5</sup>Environmental Science Program, Department of Science, Faculty of Science, Niigata University, Nishi-ku, Niigata 950-2181, Japan

<sup>6</sup>Institute for Catalysis, Hokkaido University, N21W10 Kita-ku, Sapporo, Hokkaido 001-0021, Japan & Department of Chemistry, Graduate School of Science and Engineering, Tokyo Metropolitan University, 1-1 Minami-Osawa, Hachioji Tokyo 192-0397, Japan

<sup>7</sup>Center for Computational Sciences, University of Tsukuba, Tsukuba, 305-8577, Japan & National Astronomical Observatory of Japan, Tokyo 181-8588, Japan

<sup>8</sup>Department of Astronomy, University of Virginia, Charlottesville, VA 22904, USA

### ABSTRACT

It is speculated that there might be some linkage between interstellar aldehydes and their corresponding alcohols. Here, an observational study and astrochemical modeling are coupled together to illustrate the connection between them. The ALMA cycle 4 data of a hot molecular core, G10.47+0.03 is utilized for this study. Various aldehydes (acetaldehyde, propanal, and glycolaldehyde), alcohols (methanol and ethylene glycol), and a ketone (acetone) are identified in this source. The excitation temperatures and the column densities of these species were derived via the rotation diagram method assuming LTE conditions. An extensive investigation is carried out to understand the formation of these species. Six pairs of aldehyde-alcohol: i) methanal and methanol; ii) ethanal and ethanol; iii) propanal and 1-propanol; iv) propenal and allyl alcohol; v) propynal and propargyl alcohol; vi) glycolaldehyde and ethylene glycol; vii) along with one pair of ketone-alcohol (acetone and isopropanol) and viii) ketene-alcohol (ethenone and vinyl alcohol) are considered for this study. Two successive hydrogenation reactions in the ice phase are examined to form these alcohols from aldehydes, ketone, and ketene, respectively. Quantum chemical methods are extensively executed to review the ice phase formation route and the kinetics of these species. Based on the obtained kinetic data, astrochemical modeling is employed to derive the abundances of these aldehydes, alcohols, ketone, and ketene in this source. It is seen that our model could successfully explain the observed abundances of various species in this hot molecular core.

**Keywords:** Astrochemistry, ISM: molecules – molecular data – molecular processes, ISM: abundances, ISM: evolution

### 1. INTRODUCTION

More than 200 molecular species have been identified in the interstellar medium (ISM) and circumstellar shells (McGuire 2018, <https://cdms.astro.uni-koeln.de/classic/molecules>), which resolved the much-unexplained mystery of the molecular Universe. Interstellar grains accelerate the formation of Complex Organic Molecules (COMs, molecule with > 6 atoms) in space. During the warm-up phase of a star-forming core, radicals or simple molecules on the grain surface become mobile and could produce var-

ious COMs (Chakrabarti et al. 2006a,b; Garrod & Herbst 2006; Garrod et al. 2008; Das et al. 2008a, 2010; Das & Chakrabarti 2011; Das et al. 2016; Sil et al. 2018). These ice phase species may transfer to the gas phase by various desorption mechanisms.

Alcohols and aldehydes were identified in various parts of the ISM. Methanal (formaldehyde, H<sub>2</sub>CO) is the simplest form of aldehydes, which was first observed in space by Snyder et al. (1969). It is an intermediary of the large complex organic molecules, which can help constrain physical conditions in the star-forming regions (Persson et al. 2018). Methanol (methyl alcohol, CH<sub>3</sub>OH) is the simplest alcohol and is one of the most abundant interstellar molecules. It was widely observed toward various sources (Allamandola et al. 1992; Pontoppidan et al. 2003) and is used as a

reliable tracer of high-density environments (Menten et al. 1988). A wide number of studies reported the chemical origin of methanol starting from formaldehyde (Watanabe & Kouchi 2002; Fuchs et al. 2009; Goumans 2011; Song & Kästner 2017). Methanol is ubiquitous in star-forming regions (Weaver et al. 2018) and is mainly formed on the interstellar dust via successive hydrogen addition reactions with carbon monoxide (Fedoseev et al. 2015; Chuang et al. 2016; Butscher et al. 2017).

Woon (2002a) carried out a theoretical study of the formation of  $\text{H}_2\text{CO}$  and  $\text{CH}_3\text{OH}$ . Quantum chemical calculations were carried out to determine the activation barrier for the hydrogen addition reactions ( $\text{H} + \text{CO}$  and  $\text{H} + \text{H}_2\text{CO}$ ) in gas, with water clusters  $(\text{H}_2\text{O})_n$  ( $n \leq 3$ ) and in ice phases. He included explicit water molecules to show the catalytic effect on the activation barrier by surrounding water molecules. Rimola et al. (2014); Das et al. (2008b) studied methanol formation by successive hydrogen addition with CO in water ice. They compared their simulated abundance with observations. Recently, Song & Kästner (2017) derived the tunneling rate constant of  $\text{H}_2\text{CO} + \text{H}$  reaction on amorphous solid water for various product channels:  $\text{CH}_2\text{OH}$ ,  $\text{CH}_3\text{O}$ , and  $\text{H}_2 + \text{HCO}$ . They also provided the activation barrier of these three product channels and rate coefficients.

Identification of ethanal ( $\text{CH}_3\text{CHO}$ , acetaldehyde) was first reported by Gottlieb (1973) toward Sgr B2 and Sgr A. They reported an emission at 1065 MHz, which was assigned to the  $1_{10} \rightarrow 1_{11}$  transition of  $\text{CH}_3\text{CHO}$ . This assignment was based on the agreement in radial velocity with other molecules, which were observed in the galactic center region. Then Fourikis et al. (1974) observed it toward Sgr B2 with the Parkes 64m telescope. Its successor, ethanol ( $\text{C}_2\text{H}_5\text{OH}$ , ethyl alcohol), is among the earliest complex molecules, which was identified toward the Sgr B2 (Zuckerman et al. 1975).

Propanal ( $\text{CH}_3\text{CH}_2\text{CHO}$ , propionaldehyde) is identified in Sgr B2(N) (Hollis et al. 2004), where it coexists with propynal ( $\text{HC}_2\text{CHO}$ ) and propenal ( $\text{CH}_2\text{CHCHO}$ ). The detection of these three aldehydes toward the same source suggests that successive hydrogen additions might be an efficient process to establish the chemical linkage between propynal, propenal, and propanal (Hollis et al. 2004). Propenal (also known as acrolein) is the simplest unsaturated aldehyde. It is the second most stable isomer of the  $\text{C}_3\text{H}_4\text{O}$  isomeric group (Etim et al. 2018). Allyl alcohol ( $\text{CH}_2\text{CHCH}_2\text{OH}$ ) is an isomer of propanal and the corresponding alcohol of propenal (Zaverkin et al. 2018). Acetaldehyde is supposed to be a potential ancestor of carbohydrates and propenal (also known as acrolein) (Pizzarello & Weber 2004; Córdova et al. 2005).

The corresponding alcohol of propanal is 1-propanol ( $\text{CH}_3\text{CH}_2\text{CH}_2\text{OH}$ ), which is yet to be observed in space. However, trans-ethyl methyl ether ( $\text{CH}_3\text{CH}_2\text{OCH}_3$ ), which

is one of the isomers of the same isomeric group, was tentatively detected toward Orion KL (Tercero et al. 2015). Zaverkin et al. (2018) reported that the propanal to 1-propanol production by the hydrogenation reaction might be inefficient due to the efficient hydrogen abstraction reaction.

The simplest form of sugar, glycolaldehyde ( $\text{HOCH}_2\text{CHO}$ ), plays an essential role in forming amino acids and complex sugars (Weber 1998; Collins et al. 1995). Glycolaldehyde was also detected outside of the Galactic Center towards the hot core G31.41+0.31 (Beltrán et al. 2009) (hereafter, G31). Ethylene glycol ( $\text{HOCH}_2\text{CH}_2\text{OH}$ ) is the corresponding alcohol of glycolaldehyde. It was detected in a wide variety of sources such as in the Galactic Center (Hollis et al. 2002; Belloche et al. 2013), NGC 1333-IRAS 2A (Maury et al. 2014), Orion bar (Brouillet et al. 2015) and also in the comets C/1995 O1 (Hale-Bopp) (Crovisier et al. 2004), C/2012 F6 (Lemmon) and C/2013 R1 (Lovejoy) (Biver et al. 2014). It was also identified in the Murchinson and Murray meteorites (Cooper et al. 2001). The abundance ratio of glycolaldehyde and ethylene glycol in star-forming regions and comets can help understand the possible preservation of complex organic molecules (Coutens et al. 2018). Methyl formate ( $\text{CH}_3\text{OCHO}$ ) and acetic acid ( $\text{CH}_3\text{COOH}$ ) are two isomers of glycolaldehyde. The linkage between the methyl formate, acetic acid, and glycolaldehyde can constrain the understanding of the chemical and physical conditions of the star-forming core (Woods et al. 2013). Acetone ( $\text{CH}_3\text{COCH}_3$ ) is one of the most important molecules in organic chemistry, and it was the first species containing 10 atoms identified in the ISM (Combes et al. 1987). Acetone was also found to be present in the comet 67P/Churyumov-Gerasimenko (Altwegg et al. 2017). Ethenone ( $\text{CH}_2\text{CO}$ , ketene) was identified for the first time toward Sgr B2(OH) by Turner (1977) through microwave measurements. Recently, Turner et al. (2020) perform experiment combined with high-level quantum chemical calculations and provide compelling evidence of ketene formation in the processed mixture of water and carbon monoxide ices explaining the observed ketene detection in deep space. The simplest enol compound, vinyl alcohol ( $\text{CH}_2\text{CHOH}$ , ethenol), was identified in an interstellar cloud of dust and gas near the center of the Milky Way galaxy toward Sgr B2(N) utilizing its millimeter-wave rotational transitions (Turner & Apponi 2001). In the dark cloud, the non-energetic process plays an active role in processing the ice constituents. In contrast, in the latter stages of star and planet formation, various energetic procedures play a crucial role (Fedoseev et al. 2017). Laboratory experiments of methanol dissociation studied through various energetic processes, such as photons, electrons, Vacuum Ultraviolet (VUV) photons, X-ray, etc. that could lead to the synthesis of various COMs. Öberg et al. (2009) found that the ratio between ethylene glycol to ethanol

and methyl formate to ethanol varies with the ice temperature and irradiation.

In this work, ALMA archival data of a hot molecular core, G10.47+0.03 is analyzed which is located at a distance of 8.6 kpc (Sanna et al. 2014). This is a young cluster (Cesaroni et al. 1998; Rolffs et al. 2011) whose luminosity is  $\sim 5 \times 10^5 L_{\odot}$  (Cesaroni et al. 2010). Many simple species, complex organics, and molecules with higher upper energy state (such as HC<sub>3</sub>N, HCN) were observed in this source, suggesting an active site for the chemical enrichment (Ikeda et al. 2001; Wyrowski et al. 1999; Gibb et al. 2004; Rolffs et al. 2011; Gorai et al. 2020).

Recently Qasim et al. (2019) showed that the aldehyde and primary alcohol may be linked via successive hydrogen addition reactions. A similar connection is also observed between ketones and secondary alcohols, i.e., isopropanol (CH<sub>3</sub>CHOHCH<sub>3</sub>) can be synthesized via two successive hydrogen additions with acetone (Hiraoka et al. 1998). Here, several aldehydes and alcohols are identified. Obtained column density, rotation temperature, spatial distributions of these molecules are discussed to understand the morphological correlation between these aldehydes and alcohols. The astrochemical model is implemented to compare with the observational finding. This work demonstrates that consecutive hydrogen addition could contribute to forming some complex interstellar molecules. Here, the kinetics of the consecutive hydrogen addition reactions of alcohol production from aldehyde, ketone, and ketene are examined. Binding energies (BEs) of a species with a grain substrate are essential for constructing a chemical model. Most COMs are primarily produced on the dust surface and further desorbed back to the gas phase (Requena-Torres et al. 2006). Most of the time, BE of these species is estimated, which may induce uncertainties in the results. Our estimated BE values with the water ice surface are included in our chemical model to see their impact. The proton affinity (PA) is not directly included in our model. But it is computed to check the reactivity of these species with H<sup>+</sup>. The role of PA of various species and their intermediate steps is also discussed to synthesize new COMs. Some of our obtained kinetic parameters are directly included in our chemical model to compare between the observation and modeling yields.

The remainder of this paper is organized as follows. In Section 2, the observational results are presented. The computational details adopted to explain the chemical linkage between aldehyde and alcohol are given in Section 3. Astro-

chemical modeling and its implication are discussed in Section 4 and finally in Section 5, we conclude.

## 2. OBSERVATIONS OF A HOT MOLECULAR CORE, G10.47+0.03

### 2.1. Observations and data analysis

This paper uses the ALMA cycle 4 archival data (12m array data) of the observations (#2016.1.00929.S) of G10.47+0.03 (hereafter, G10). The pointing center of the G10 observations is located at  $\alpha(J2000) = 18^{\text{h}}08^{\text{m}}38^{\text{s}}.232$ ,  $\delta(J2000) = -19^{\circ}51'50''.4$ . This observation was performed with band 4 having four spectral bands covering the sky frequencies of 129.50 – 131.44 GHz, 147.50 – 149.43 GHz, 153.00 – 154.93 GHz, and 158.49 – 160.43 GHz and corresponding angular resolution at four different frequencies are 1.67'' (14362 AU), 1.52'' (13072 AU), 1.66'' (14276 AU), and 1.76'' (15136 AU) respectively. The spectral resolution of the data is 976 kHz. The number of antennas used for the corresponding four spectral windows are 39, 40, 41 and 39, respectively. The flux calibrator, phase calibrator, and band-pass calibrator of this observation were J1733-1304, J1832-2039, and J1924-2914. The systemic velocity of the source is 68 km s<sup>-1</sup> (Rolffs et al. 2011). A detailed description of the observations was presented in Gorai et al. (2020). Here, all the analysis (spectral and line analysis) are carried out by using CASA 4.7.2 software (McMullin et al. 2007). Since G10 is a line-rich source, the corrected sigma-clipping method of the STATCONT package (Sánchez-Monge et al. 2018) are used to determine the continuum level in data cube. Further, the spectral window of the data cube is divided into two data cubes (continuum and line emission), using the ‘uvcontsub’ command in the CASA program. Line identification is performed with the CASSIS (Vastel et al. 2015) (This software has been developed by IRAP-UPS/CNRS (<http://cassis.irap.omp.eu>), which uses the Cologne Database for Molecular Spectroscopy (CDMS<sup>1</sup>, Müller et al. 2001, 2005; Endres et al. 2016) and Jet Propulsion Laboratory (JPL<sup>2</sup>, Pickett et al. 1998) databases. Various physical parameters ( $V_{\text{LSR}}$ , line blending, upper-state energy, Einstein coefficient, and 3 sigma significance level) are considered. LTE synthetic spectra are generated with the best-fitted parameters to compare the observed spectral feature and line identification. We have also used the <https://splatalogue.online> for the additional confirmation of our choices.

<sup>1</sup> <https://cdms.astro.uni-koeln.de>

<sup>2</sup> <https://spec.jpl.nasa.gov>

**Table 1.** Summary of the line parameters of the observed molecules toward G10.47+0.03.

Species	$J'_{K'_a K'_c} - J''_{K''_a K''_c}$	Frequency (GHz)	$E_u$ (K)	$\Delta V$ (km s <sup>-1</sup> )	$I_{max}$ (K)	$V_{LSR}$ (km s <sup>-1</sup> )	$S\mu^2$ (Debye <sup>2</sup> )	$\int T_{mb} dV$ (K km s <sup>-1</sup> )
Methanol (CH <sub>3</sub> OH)	21 <sub>-0,21</sub> - 21 <sub>1,21</sub> E, vt=0	129.720384	546.2	9.6±0.2	30.1±0.6	66.9±0.1	19.8	308.7±14.5
	17 <sub>-4,13</sub> - 18 <sub>-3,16</sub> E, vt=0	131.134094	450.9	11.1±0.2	45.7±0.5	66.6±0.5	21.8	540.0±17.7
	7 <sub>-1,7</sub> - 6 <sub>0,6</sub> E, vt=1	147.943673	356.3	11.1±0.8	32.1±1.9	66.2±0.4	14.4	378.5±52.8
	15 <sub>-0,15</sub> - 15 <sub>1,15</sub> E, vt=0	148.111993	290.7	10.5±0.6	44.7±1.5	66.5±0.2	29.02	500.0±47.2
	8 <sub>-7,1</sub> - 7 <sub>-6,1</sub> E, vt=1	153.128697	664.5	10.4±0.2	9.15±0.1	66.8±0.1	15.9	101.1±3.1
	12 <sub>-0,12</sub> - 15 <sub>1,12</sub> E, vt=0	153.281282*	193.8	11.37±0.2	40.28±0.6	66.3±0.1	30.7	487.4±14.5
11 <sub>-0,11</sub> - 11 <sub>1,11</sub> E, vt=0	154.425832*	166.1	10.6±0.3	36.02±0.7	66.64±0.1	30.5	408.0±18.7	
Ethylene Glycol (CH <sub>2</sub> OH) <sub>2</sub>	33 <sub>10,23</sub> - 32 <sub>11,22</sub> , 1-1	130.115657	323	7.7±0.07	2.55±0.01	67.8± 0.03	53	20.9±0.3
	13 <sub>9,4</sub> - 12 <sub>9,3</sub> , 0-1	130.998583	83.7	7.9±0.5	5.6±0.24	68.2±0.178	98.4	48.1±5.02
	28 <sub>7,21</sub> - 28 <sub>6,23</sub> , 1-0	131.229156	223.4	7.8±0.1	4.8±0.02	68.8± 0.04	158.3	39.8±0.7
	27 <sub>3,25</sub> - 27 <sub>2,26</sub> , 0-0	148.082465	185.5	7.2±0.13	4.8±0.15	69.3±0.12	87.3	36.89±1.8
	39 <sub>8,32</sub> - 39 <sub>7,33</sub> , 1-1	153.325448	414	10.5±0.5	3.9±0.1	69.4±0.15	385.1	44.14±3.13
	8 <sub>4,5</sub> - 7 <sub>3,5</sub> , 1-0	153.567383	25.4	8.9±0.27	13.8±0.33	66.9±0.11	60.4	131.45±7.08
13 <sub>3,11</sub> - 12 <sub>2,10</sub> , 0-0	159.768239	48.8	8.73±0.25	9.32±0.15	68.4±0.08	62.8	86.65±3.87	
Acetaldehyde (CH <sub>3</sub> CHO)	8 <sub>5,4</sub> - 7 <sub>5,3</sub> , A	154.161467	89.8	7.3±0.7	5.0±0.4	67.6±0.3	61.7	38.8±0.10
	8 <sub>3,5</sub> - 7 <sub>3,4</sub> , A	154.173895	114.4	6.6±0.2	1.3±0.1	67.8±0.1	44.3	9.2±0.53
	8 <sub>4,4</sub> - 7 <sub>4,3</sub> , A	154.201471	69.5	8.8±0.5	5.7±0.2	67.0±0.2	75.9	52.9±0.08
	8 <sub>3,6</sub> - 7 <sub>3,5</sub> , A	154.274686	53.7	8.4±0.2	5.3±0.1	67.1±0.7	87.0	47.5±0.01
	8 <sub>3,5</sub> - 7 <sub>3,4</sub> , E	154.296489	53.7	8.3±0.2	4.5±0.1	66.8±0.1	87.0	39.6±0.03
Propanal (CH <sub>3</sub> CH <sub>2</sub> CHO)	10 <sub>7,4</sub> - 10 <sub>6,5</sub> , A	147.867697	54.6	12.1±1.2	12.3±0.8	68.9±0.4	12.0	158.4±6.5
	9 <sub>7,3</sub> - 9 <sub>6,4</sub> , A	148.005214	49.6	10.1±0.3	11.5±0.3	67.6±0.1	9.3	123.8±1.5
	25 <sub>3,22</sub> - 25 <sub>2,23</sub> , A	153.554511	172.7	9.0±0.3	13.2±0.3	68.9±0.1	31.2	126.2±3.5
	27 <sub>5,23</sub> - 27 <sub>4,24</sub> , A	154.067527	206.2	8.5±0.3	13.5±0.3	69.8±0.1	41.6	123.4±3.3
	16 <sub>2,15</sub> - 15 <sub>1,14</sub> , A	159.932413	68.6	9.9±0.2	18.7±0.2	68.3±0.1	38.1	198.2±3.2
Glycolaldehyde (HOCH <sub>2</sub> CHO)	15 <sub>0,15</sub> - 14 <sub>114</sub>	153.597996	60.5	8.1±0.3	3.9±0.1	66.9±0.1	72.9	11.7±2.3
	20 <sub>7,13</sub> - 20 <sub>6,14</sub>	153.614231	147.0	7.1±0.6	2.1±0.2	66.4±0.2	60.4	11.5±2.5
Acetone (CH <sub>3</sub> COCH <sub>3</sub> )	25 <sub>10,15</sub> - 25 <sub>9,16</sub> , AE	130.708968	241	8.2±0.3	4.43±0.1	65.8±0.1	536.9	38.8± 2.1
	12 <sub>2,11</sub> - 11 <sub>1,10</sub> , AA	130.924799	44.1	10.6±0.2	7.7±0.1	66.3±0.1	876.4	86.6±2.9
	11 <sub>5,7</sub> - 10 <sub>4,6</sub> , EE	147.684364	48.4	9.6±0.2	6.13±0.1	67.5±0.1	783.8	62.7±2.5
	26 <sub>10,17</sub> - 26 <sub>9,18</sub> , EE	149.190766	251	10.9±0.7	7.4±0.3	65.5±0.2	1309.1	86.1±8.2
	13 <sub>2,11</sub> - 12 <sub>3,10</sub> , AE	149.395864	55.8	10.8±1.1	8.4±0.5	68.3±0.4	517.6	96.7±15.7
	14 <sub>2,12</sub> - 13 <sub>3,11</sub> , EE	159.247634	63	8.7±0.2	14.8±0.2	67.5±0.1	1516.9	137.3±5.5
	24 <sub>6,18</sub> - 24 <sub>5,19</sub> , EE	159.415955	198	8.8±0.2	9.6±0.1	68.4± 0.1	902.1	89.16±2.6
22 <sub>4,18</sub> - 22 <sub>3,19</sub> , EE	160.118153	157.1	9.3±0.2	4.3±0.1	65.5±0.1	607.6	42.4±2.0	
Methyl formate (CH <sub>3</sub> OCHO)	11 <sub>2,10</sub> - 10 <sub>2,9</sub> , A	130.016790	40.7	9.5±0.20	17.55±0.3	66.1±0.07	28.04	178.3±6.44
	11 <sub>2,10</sub> - 10 <sub>2,9</sub> , E	130.010105	40.7	9.4±0.17	17.14±0.12	66.4±0.04	28.04	171.7±4.46
	12 <sub>1,12</sub> - 11 <sub>1,11</sub> , A	131.377495	230	9.38±0.2	6.28±0.05	66.7±0.05	31.39	62.7±1.83
	12 <sub>4,8</sub> - 11 <sub>4,7</sub> , E	148.575217	244.1	8.65±0.9	8.13±0.73	66.9±0.4	28.3	74.87±14.48
	12 <sub>4,9</sub> - 11 <sub>4,8</sub> , A	148.805941	56.8	8.52±0.44	18.13±0.7	66.3±0.2	28.4	164.50±14.98

Table 1 continued

Table 1 (continued)

Species	$J'_{K'_a K'_c} - J''_{K''_a K''_c}$	Frequency (GHz)	$E_u$ (K)	$\Delta V$ (km s <sup>-1</sup> )	$I_{max}$ (K)	$V_{LSR}$ (km s <sup>-1</sup> )	$S\mu^2$ (Debye <sup>2</sup> )	$\int T_{mb}dV$ (K km s <sup>-1</sup> )
	13 <sub>3,11</sub> – 12 <sub>3,10</sub> , A	158.704392	59.6	9.4±0.2	24.29±0.4	66.2±0.1	32.57	243.05±9.17
	13 <sub>10,4</sub> – 12 <sub>10,3</sub> , A	159.662793	120.04	8.71±0.3	18.78±0.3	66.64±0.07	14.1	174.12±4.38
	13 <sub>7,6</sub> – 12 <sub>7,5</sub> , A	160.178942	86.2	9.03±0.25	16.05±0.22	66.4±0.08	24.5	154.27±6.30
	13 <sub>7,6</sub> – 12 <sub>7,5</sub> , A	160.193496	86.2	9.5±0.15	35.15±0.32	66.48±0.04	24.5	358.00±3.00
Dimethyl ether (CH <sub>3</sub> OCH <sub>3</sub> )	6 <sub>1,6</sub> – 5 <sub>0,5</sub> , EE	131.405796	19.9	11.8±0.5	28.7±0.5	66.1±0.2	82.4	359.9±20.6
	9 <sub>0,9</sub> – 8 <sub>1,8</sub> , EE	153.054818	40.4	9.4±0.2	26.5±0.3	66.8±0.1	126.4	264.02±6.5
	24 <sub>4,20</sub> – 24 <sub>3,21</sub> , EE	153.385902	297.5	12.4±0.4	11.5±0.1	67.2±0.1	379.5	151.6±3.6
	11 <sub>1,10</sub> – 10 <sub>2,9</sub> , EE	154.455083	62.9	10.6±0.2	11.6±0.1	66.1±0.1	68.8	130.3±3.7

NOTE—\* optically thick

## 2.2. Synthesized images

Continuum maps at 1.88 mm, 1.94 mm, 2.02 mm, and 2.30 mm were presented in Gorai et al. (2020). They obtained the corresponding synthesized beam and position angle  $2.38'' \times 1.39''$  and  $77.84^\circ$ ;  $2.03'' \times 1.47''$  and  $73.50^\circ$ ;  $1.98'' \times 1.57''$  and  $64.28^\circ$ ; and  $2.44'' \times 1.64''$  and  $63.16^\circ$ , respectively. Others parameters of continuum images such as frequency, peak flux, integrated flux, and deconvolved beam size (FWHM) were presented in Table 2 of Gorai et al. (2020). The synthesized beam size of this data cube was not sufficient to resolve the continuum emission. Hydrogen column density and dust optical depth of each continuum map was presented in Table 4 of Gorai et al. (2020). The average value of hydrogen column density is  $\sim 1.35 \times 10^{25} \text{ cm}^{-2}$  and dust optical depth is 0.136 implies that the source as optically thin (Gorai et al. 2020).

## 2.3. Line analysis

The observed spectra obtained within the circular region having a diameter of  $2.0''$  ( $\sim 17200$  AU) centered at RA (J2000) =  $(18^{\text{h}}08^{\text{m}}38^{\text{s}}.232)$ , Dec (J2000) =  $(-19^\circ 51' 50''.4)$  are continuum subtracted for the analysis. The line width ( $\Delta V$ ), the LSR velocity ( $V_{LSR}$ ), and the integrated intensity ( $\int T_{mb}dV$ ) of the each transition which is obtained after Gaussian fitting to the observed transition is noted. All the line parameters corresponding to a observed transition such as associated quantum numbers  $J'_{K'_a K'_c} - J''_{K''_a K''_c}$ , rest frequency ( $\nu_0$ ),  $\Delta V$ ,  $\int T_{mb}dV$ , upper state energy ( $E_u$ ),  $V_{LSR}$  are presented in Table 1. Multiple transitions of methanol (CH<sub>3</sub>OH), acetaldehyde (CH<sub>3</sub>CHO), ethylene glycol [(CH<sub>2</sub>OH)<sub>2</sub>], glycolaldehyde (HOCH<sub>2</sub>CHO), propanal (CH<sub>3</sub>CH<sub>2</sub>CHO), acetone (CH<sub>3</sub>COCH<sub>3</sub>), methyl formate (CH<sub>3</sub>COH), and dimethyl ether (CH<sub>3</sub>OCH<sub>3</sub>) are identified. This is the first time, ethylene glycol and propanal are identified in G10. Only two lines of glycolaldehyde are identified. Therefore, it is considered as the tentative detection in this source. The observed spectra of these species and

fitted spectra are shown in the Appendix (see Figure B1). The integrated intensity for the methanol, ethylene glycol, and glycolaldehyde is obtained by simple Gaussian fitting to each transition. In the case of acetaldehyde, propanal, acetone, methyl formate, and dimethyl ether, torsional sub-states due to the internal rotation of the methyl group are noticed. For acetone and dimethyl ether, these sub-states are AA, EE, EA, and AE. In the case of acetaldehyde, propanal, and methyl formate, A and E sub-states are noticed. But these transitions are found to be blended with different sub-states. These transitions were not resolved due to the low spectral resolution of the present spectra. The integrated intensity is obtained with the Gaussian fitting and then dividing this integrated intensity according to their  $S\mu^2$  values (obtained from <https://www.cv.nrao.edu/php/splat>). The transition having maximum intensity between the torsional sub-states was considered in the rotation diagram analysis to calculate the rotation temperature and column density.

## 2.4. Spatial distribution of aldehydes and alcohols

The integrated intensity distribution of CH<sub>3</sub>OH, CH<sub>3</sub>CHO, (CH<sub>2</sub>OH)<sub>2</sub>, HOCH<sub>2</sub>CHO, CH<sub>3</sub>CH<sub>2</sub>CHO, CH<sub>3</sub>COCH<sub>3</sub>, CH<sub>3</sub>COH, and CH<sub>3</sub>OCH<sub>3</sub> are shown in Appendix (see Figures C1–C4). The source sizes are determined by using two-dimensional Gaussian fitting of the images. The deconvolved beam size of the emitting region is estimated as  $\theta_s = \sqrt{\theta_{50}^2 - \theta_{beam}^2}$ , where  $\theta_{50} = 2\sqrt{A/\pi}$  is diameter of the circle whose area (A) enclosing 50% line peak and  $\theta_{beam}$  is the half-power width of the synthesized beam (Rivilla et al. 2017). It is noticed that all the lines have their peak around the position of the continuum. The emitting diameter of the observed species is summarized in Table A1. It is noticed that the emitting diameters of different observed transitions are smaller than the beam size. So all these transitions are not well spatially resolved or, at best, marginally resolved. In the case of methanol, the emitting region varies from  $1.23''$  to  $1.81''$ , and it is noticed that the emitting regions of

**Table 2.** Estimated rotation temperature and column density of the observed molecules in G10. In the last column, the obtained column densities are compared with other observations of G10.

Molecule	$T_{rot}$ [K]	$N_{tot}$ [cm <sup>-2</sup> ] <sup>a</sup>	Literature $N_{tot}$ [cm <sup>-2</sup> ]
CH <sub>3</sub> OH	206 ± 66	$(4.3 ± 3.4) × 10^{18}$	$9.0 × 10^{18b}$
(CH <sub>2</sub> OH) <sub>2</sub>	185 ± 61	$(5.0 ± 2.1) × 10^{17}$	
CH <sub>3</sub> CHO	72 ± 11	$(6.8 ± 1.1) × 10^{15}$	$(2.1 ± 0.7) × 10^{14c}$
CH <sub>3</sub> CH <sub>2</sub> CHO	234 ± 42	$(2.4 ± 0.23) × 10^{17}$	
HOCH <sub>2</sub> CHO	155	$1.3 × 10^{16}$	
CH <sub>3</sub> COCH <sub>3</sub>	224 ± 41	$(5.4 ± 0.7) × 10^{17}$	$5.0 × 10^{17b}$
CH <sub>3</sub> OCHO	191 ± 24	$(9.1 ± 0.7) × 10^{17}$	$7.0 × 10^{17b}$
CH <sub>3</sub> OCH <sub>3</sub>	148 ± 42	$(1.5 ± 0.4) × 10^{17}$	$1.5 × 10^{18b}$

NOTE— Estimated values have 12–33% and 8–79% uncertainty for temperature and column density, respectively.

<sup>a</sup> This work.

<sup>b</sup> (Rolfis et al. 2011,  $\theta_b = 0.28 - 4.27''$ ,  $\theta_s = 1.5''$ ,  $T_{ex} = 200$  K),

<sup>c</sup> (Ikeda et al. 2001,  $\theta_b = 16 - 26'$ ,  $\theta_s = 20'$ ,  $T_{rot} = 30 ± 4$  K)

methanol decrease with an increase of upper state energy. Therefore, methanol could trace the temperature distribution of the source. However, our data cannot provide much insight into the source's temperature distributions due to the low angular resolution. All transitions of acetaldehyde having upper state energy < 100 K are detected from the 1.33'' – 1.53'' region. The emitting region of dimethyl ether and methyl formate transitions having upper state energy < 100 K varies between 1.83'' – 1.95'' and 1.66'' – 1.95'', respectively. So, dimethyl ether and methyl formate transitions are found from roughly the similar region as acetaldehyde. But the transitions of propanal, glycolaldehyde, acetone, and ethylene glycol are detected from different positions. It is observed that the transitions of propanal, glycolaldehyde, and ethylene glycol emissions are very compact toward the dust continuum except for some transitions. These suggest the grain surface origin of these species. Emissions of dimethyl ether and methyl formate are found to be comparatively extended compared to the other species. The emitting region of ethylene glycol is small compared to the emission of all other COMs identified in this work. The emitting region of dimethyl ether is found to be more extensive compared to all other species.

### 2.5. Rotation diagram analysis

Here, a rotational diagram analysis is performed by assuming the observed transitions are optically thin and in Local Thermodynamic Equilibrium (LTE). For optically thin lines, column density can be expressed as (Goldsmith & Langer 1999),

$$\frac{N_u^{thin}}{g_u} = \frac{3k_B \int T_{mb} dV}{8\pi^3 \nu S \mu^2}, \quad (1)$$

where,  $g_u$  is the degeneracy of the upper state,  $k_B$  is the Boltzmann constant,  $\int T_{mb} dV$  is the integrated intensity,  $\nu$  is the rest frequency,  $\mu$  is the electric dipole moment, and  $S$  is the line strength. Under LTE condition, the total column density would be written as,

$$\frac{N_u^{thin}}{g_u} = \frac{N_{total}}{Q(T_{rot})} \exp^{-E_u/k_B T_{rot}}, \quad (2)$$

where,  $T_{rot}$  is the rotational temperature,  $E_u$  is the upper state energy,  $Q(T_{rot})$  is the partition function at rotational temperature. The above two equations can be rearranged as,

$$\ln\left(\frac{N_u^{thin}}{g_u}\right) = -\left(\frac{1}{T_{rot}}\right)\left(\frac{E_u}{k_B}\right) + \ln\left(\frac{N_{total}}{Q(T_{rot})}\right). \quad (3)$$

The rotational temperature and total column density of a species are simultaneously determined from this expression. All the spectroscopic parameters for this analysis are taken either from the Cologne Database for Molecular Spectroscopy (CDMS, <https://cdms.astro.uni-koeln.de>, Müller et al. 2001, 2005; Endres et al. 2016) or from the Jet Propulsion Laboratory database (JPL, <http://spec.jpl.nasa.gov>, Pickett et al. 1998). Rotational diagram of methanol (CH<sub>3</sub>OH), acetaldehyde (CH<sub>3</sub>CHO), ethylene glycol [(CH<sub>2</sub>OH)<sub>2</sub>], glycolaldehyde (HOCH<sub>2</sub>CHO), propanal (CH<sub>3</sub>CH<sub>2</sub>CHO), acetone (CH<sub>3</sub>COCH<sub>3</sub>), methyl formate (CH<sub>3</sub>OCHO), and dimethyl ether (CH<sub>3</sub>OCH<sub>3</sub>) are shown in Figure 1. The derived rotational temperatures and column densities are summarized in Table 2. In Table 2, we have noted the errors. The relative percentage errors of the rotational temperature and column density are noted at the footnote of the table. The rotational diagram of glycolaldehyde is constructed with only two data points. Therefore, the rotational temperature has been assumed to some constant value. Methanol transitions with a wide range (166 K - 664 K) of upper state energies are observed. Some of these transitions are optically thick (i.e., 153.281 GHz and 154.425 GHz). Therefore, it is challenging to construct the rotation diagram with all seven unblended methanol lines (noted in Table 1). Since two transitions are optically thick, these are excluded from the rotation diagram analysis. Furthermore, by considering the rest of the five transitions, considerable uncertainty in the estimated column density  $((3.7 ± 3) × 10^{18}$  cm<sup>-2</sup>) and rotational temperature (345 ± 198 K) is obtained. Comparatively, a better linear fit was possible if we exclude the 148.111 GHz transitions from the rotation diagram (by choosing the transitions having upper state energy > 300 K). It yields a column density and rotational temperature of methanol  $(4.3 ± 3.4) × 10^{18}$  cm<sup>-2</sup> and 206 ± 66 K, respectively.

For the sample of considered molecules, our estimated rotation temperature varies from 72 K to 234 K. A low rotation temperature  $\sim 72 ± 11$  K for acetaldehyde is obtained, which is in agreement with the rotation temperature of acetaldehyde obtained by Ikeda et al. (2001). Olmi et al.

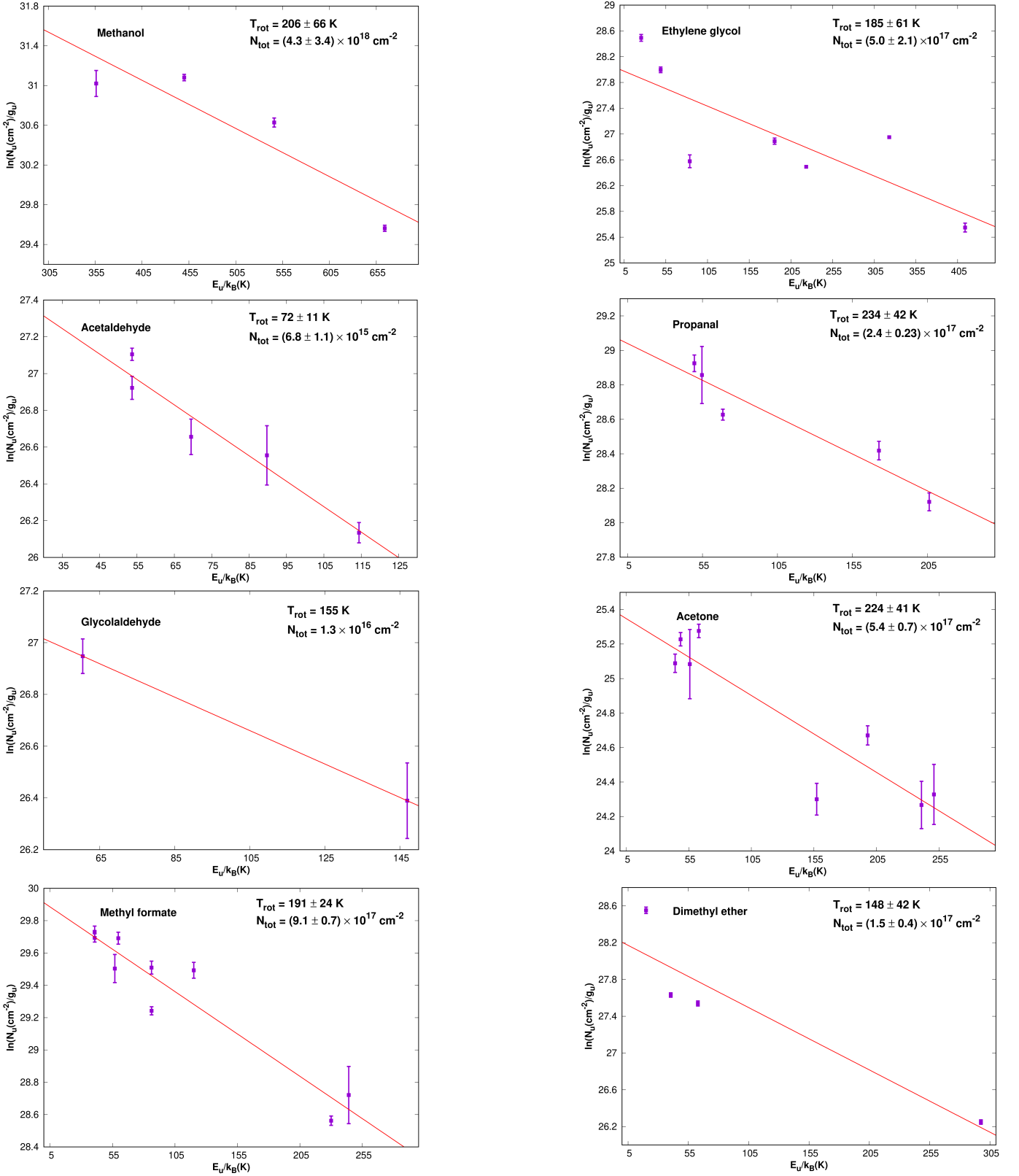


**Figure 1.** Rotation diagram of observed molecules are shown. The best fitted rotational temperature and column density are given in each panel. Filled purple squares are the data points and purple line represents the error bar.

(1996) derived a temperature of 160 K for CH<sub>3</sub>CN. Rolffs et al. (2011) considered a temperature of 200 K to give an optimum fit to the data for line identification purposes. The average rotational temperature obtained from the species observed here is 177 K, which is in close agreement with Olmi et al. (1996); Rolffs et al. (2011). There could be a possibility of beam dilution on the derived column densities and excitation temperatures. If the beam dilution effect is included in the rotation diagram, it is noticed that, on average, our column densities and temperatures would increase by a factor of 3.2 and 1.4, respectively. Derived column density and rotational temperature are further used in the LTE module of CASSIS to produce synthetic LTE spectra and also compare with our observations (see Figure B1). The average FWHM of each species from Table 1 is used for this computation. A source size of 2'' with the ALMA telescope is considered. Figure B1 shows a good agreement with the observed feature except for the three transitions of methanol and all the transitions of dimethyl ether. The intensity of the three methanol transitions is overproduced. Among them, 153.281 GHz and 154.425 GHz transitions are optically thick. All the transitions of dimethyl ether are underproduced. During the line analysis, it is noticed that these transitions consist of multiple sub-states. The strongest transition is only considered based on their  $S\mu^2$  value. Thus, the obtained FWHMs are possibly overestimated during the Gaussian fitting, which can underproduce the intensity of these transitions in Figure B1.

### 3. KINETICS OF THE ALDEHYDES, ALCOHOLS, KETONE, AND KETENE OBSERVED IN G10

Here, an extensive theoretical investigation is carried out to understand the formation mechanism of some aldehydes, alcohols, ketene, and ketone, which are observed in G10. All the quantum chemical results presented in this article are carried out using the Gaussian 09 suite of programs (Frisch et al. 2013). The Density Functional Theory (DFT) method with B3LYP functional (Becke 1993) and 6-31+G(d,p) basis set is used in computing the activation barrier and enthalpy of reactions. Both the activation and reaction energies are calculated including the harmonic zero-point vibrational energy (ZPVE) and considering a temperature of  $\sim 298.15$  K and  $\sim 1$  atmosphere pressure. A fully optimized ground-state structure is verified to be a stationary point (having non-imaginary frequency) by harmonic vibrational frequency analysis. For the transition state (TS) calculation, the QST2 method of the Gaussian 09 program is used. All the TSs are verified using the internal reaction coordinate (IRC) analysis which connects reactants and products through the minimum energy path of the potential energy surface (PES). Further, the higher-order method is employed to examine the effect on the activation barrier calculation. The single point energy calculation of the TS structure and the op-

timized structure of the reactants at CCSD(T)/aug-cc-pVTZ level is carried out. The ice mixture is considered embedded within a continuum solvation field to include the passive impact of bulk ice on the activation barrier and enthalpy of reaction. To mimic the ice phase feature, water is used as the solvent. A self-consistent reaction field (SCRf) is routinely applied in the electronic structure calculations to study the spectroscopy and thermochemistry parameters of any species in the ice phase. Explicit water molecules can also generate a more realistic (inhomogeneous) field. Since the typical size of the interstellar water cluster (numbers of water molecules required) is not known with certainty, it is preferred to use the SCRf method (Woon 2002b). The Polarizable Continuum Model (PCM) with different integral equation formalism variant (IEFPCM) as a default self-consistent reaction field (SCRf) method is used for this purpose (Cancès et al. 1997; Tomasi et al. 2005). A similar level of theory and basis set is used for the gas phase calculations. This method creates a solute cavity by overlapping spheres (Tomasi & Persico 1994; Pascual-Ahuir et al. 1987). The implicit solvation model places the molecule of interest inside a cavity in a continuous homogeneous dielectric medium (in this case, water) that represents the solvent. This method is proven to be producing convincing results for ices. The PCM model is used to consider the reaction field of bulk ice. Here, the cluster is treated explicitly to avoid spurious boundary effects. In this framework, the reaction fields issuing from a dielectric constant of 78 for water or about 100 for ice (Aragones et al. 2011) are essentially identical. Hence, the solid phase calculations and the thermochemistry parameters reported here are close to those in ice. The BE and PA of the aldehydes, ketone, ketene, and corresponding alcohols are also calculated quantum chemically discussed in Section 3.2.

#### 3.1. Rate constants

A cross-over temperature,  $T_c$  is defined as the maximum temperature below which tunneling reaction dominates and above which thermal activation reaction takes over.  $T_c$  is calculated by the following relation:

$$T_c = \frac{h\omega}{4\pi^2 k_B}, \quad (4)$$

where  $h$  is the Planck's constant,  $k_B$  is the Boltzmann constant, and  $\omega$  is the absolute value of the the imaginary frequency at the TS. For all the gas phase reactions, the transition state theory (TST) is applied. Gas-phase rate constant can be calculated by the following expression,

$$K = \left(\frac{k_B T}{hc^0}\right) \exp(-\Delta G^\ddagger/RT), \quad (5)$$

where,  $\Delta G^\ddagger$  is the Gibbs free energy of activation,  $c^0$  is the concentration ( $\sim 1$ ),  $R$  is the ideal gas constant and  $T$  is the temperature.



**Table 3.** Calculated Gibbs free energy of activation, activation barrier, and reaction enthalpy of alcohols formation via successive hydrogen addition with aldehydes, ketone, and ketene by using lower-level [B3LYP/6-31+G(d,p)] and higher-level [CCSD(T)/aug-cc-pVTZ] of theory considering 298.15 K temperature and 1 atmospheric pressure.

Serial No.	Reaction type	Reactions	Gibbs Free Energy of Activation		Activation Barrier		Enthalpy of Reaction	
			(kcal/mol)		(kcal/mol)		(kcal/mol)	
			Gas Phase	Ice Phase	Gas Phase	Ice Phase	Gas Phase	Ice Phase
Methanal - Methanol								
1a.	(NR)	$\text{H}_2\text{CO} + \text{H} \rightarrow \text{CH}_2\text{OH}$	10.57	11.32	5.59 (9.35) <sup>a</sup> [10.35] <sup>i</sup>	6.49 (10.02) <sup>a</sup> [11.16] <sup>j</sup>	-32.31	-32.39
1b.	(RR)	$\text{CH}_2\text{OH} + \text{H} \rightarrow \text{CH}_3\text{OH}$	...	...	0.00	0.00	-94.75	-94.93
2a.	(NR)	$\text{H}_2\text{CO} + \text{H} \rightarrow \text{CH}_3\text{O}$	7.10	6.97	1.89 (3.35) <sup>a</sup> [4.29] <sup>i</sup>	1.76 (3.10) <sup>a</sup> [3.26] <sup>j</sup>	-27.61	-27.07
2b.	(RR)	$\text{CH}_3\text{O} + \text{H} \rightarrow \text{CH}_3\text{OH}$	...	...	0.00	0.00	-99.44	-100.24
Ethanal - Ethanol								
3a.	(NR)	$\text{CH}_3\text{CHO} + \text{H} \rightarrow \text{CH}_3\text{CHOH}$	11.41	12.44	5.91 (9.38) <sup>a</sup>	6.91 (10.24) <sup>a</sup>	-27.96	-26.80
3b.	(RR)	$\text{CH}_3\text{CHOH} + \text{H} \rightarrow \text{CH}_3\text{CH}_2\text{OH}$	...	...	0.00	0.00	-92.61	-93.21
4a.	(NR)	$\text{CH}_3\text{CHO} + \text{H} \rightarrow \text{CH}_3\text{CH}_2\text{O}$	10.10	10.24	4.11 (5.36) <sup>a</sup>	4.25 (5.38) <sup>a</sup>	-21.50	-20.27
4b.	(RR)	$\text{CH}_3\text{CH}_2\text{O} + \text{H} \rightarrow \text{CH}_3\text{CH}_2\text{OH}$	...	...	0.00	0.00	-99.07	-99.74
Propanal - 1-Propanol								
5a.	(NR)	$\text{CH}_3\text{CH}_2\text{CHO} + \text{H} \rightarrow \text{CH}_3\text{CH}_2\text{CHOH}$	11.12	12.08	5.47 (9.27) <sup>a</sup> [9.82] <sup>ii</sup>	6.41 (9.87) <sup>a</sup>	-28.10 [-26.31] <sup>ii</sup>	-18.42
5b.	(RR)	$\text{CH}_3\text{CH}_2\text{CHOH} + \text{H} \rightarrow \text{CH}_3\text{CH}_2\text{CH}_2\text{OH}$	...	...	0.00	0.00	-92.82	-101.80
6a.	(NR)	$\text{CH}_3\text{CH}_2\text{CHO} + \text{H} \rightarrow \text{CH}_3\text{CH}_2\text{CH}_2\text{O}$	10.08	10.27	3.99 (4.97) <sup>a</sup> [5.71] <sup>ii</sup>	4.19 (4.96) <sup>a</sup>	-22.00 [-19.74] <sup>ii</sup>	-20.76
6b.	(RR)	$\text{CH}_3\text{CH}_2\text{CH}_2\text{O} + \text{H} \rightarrow \text{CH}_3\text{CH}_2\text{CH}_2\text{OH}$	...	...	0.00	0.00	-98.91	-99.46
Propenal - Allyl alcohol								
7a.	(NR)	$\text{CH}_2\text{CHCHO} + \text{H} \rightarrow \text{CH}_2\text{CHCHOH}$	9.56	10.48	4.00(6.30) <sup>a</sup> [7.89] <sup>ii</sup>	2.36 (10.47) <sup>a</sup>	-40.29 [-38.93] <sup>ii</sup>	-39.59
7b.	(RR)	$\text{CH}_2\text{CHCHOH} + \text{H} \rightarrow \text{CH}_2\text{CHCH}_2\text{OH}$	...	...	0.00	0.00	-76.72	-77.07
8a.	(NR)	$\text{CH}_2\text{CHCHO} + \text{H} \rightarrow \text{CH}_2\text{CHCH}_2\text{O}$	10.32	10.24	4.43 (5.79) <sup>a</sup> [6.43] <sup>ii</sup>	4.38 (6.60) <sup>a</sup>	-18.00 [-16.16] <sup>ii</sup>	-16.72
8b.	(RR)	$\text{CH}_2\text{CHCH}_2\text{O} + \text{H} \rightarrow \text{CH}_2\text{CHCH}_2\text{OH}$	...	...	0.00	0.00	-99.00	-99.95
Propynal - Propargyl alcohol								
9a.	(NR)	$\text{HC}_2\text{CHO} + \text{H} \rightarrow \text{HC}_2\text{CHOH}$	8.86	9.65	3.41 [7.41] <sup>ii</sup>	4.20 (8.28) <sup>a</sup>	-43.92 [-42.42] <sup>ii</sup>	-43.22
9b.	(RR)	$\text{HC}_2\text{CHOH} + \text{H} \rightarrow \text{HC}_2\text{CH}_2\text{OH}$	...	...	0.00	0.00	-79.53	-80.44
10a.	(NR)	$\text{HC}_2\text{CHO} + \text{H} \rightarrow \text{HC}_2\text{CH}_2\text{O}$	9.63	9.47	3.74 [5.78] <sup>ii</sup>	3.59 (5.68) <sup>a</sup>	-22.42 [-21.00] <sup>ii</sup>	-22.20
10b.	(RR)	$\text{HC}_2\text{CH}_2\text{O} + \text{H} \rightarrow \text{HC}_2\text{CH}_2\text{OH}$	...	...	0.00	0.00	-101.02	-101.46
Glycolaldehyde - Ethylene glycol								
11a.	(NR)	$\text{HOCH}_2\text{CHO} + \text{H} \rightarrow \text{HOCH}_2\text{CHOH}$	11.42	12.31	5.50 (8.75) <sup>a</sup> [9.51] <sup>iii</sup>	6.32 (9.29) <sup>a</sup>	-29.43	-30.43
11b.	(RR)	$\text{HOCH}_2\text{CHOH} + \text{H} \rightarrow \text{HOCH}_2\text{CH}_2\text{OH}$	...	...	0.00	0.00	-92.18	-92.44
12a.	(NR)	$\text{HOCH}_2\text{CHO} + \text{H} \rightarrow \text{HOCH}_2\text{CH}_2\text{O}$	9.43	9.67	3.34 (4.47)[4.97] <sup>iii</sup>	3.38 (4.17) <sup>a</sup>	-22.38	-22.61
12b.	(RR)	$\text{HOCH}_2\text{CH}_2\text{O} + \text{H} \rightarrow \text{HOCH}_2\text{CH}_2\text{OH}$	...	...	0.00	0.00	-99.22	-100.25
Acetone - Isopropanol								
13a.	(NR)	$\text{CH}_3\text{COCH}_3 + \text{H} \rightarrow \text{CH}_3\text{COHCH}_3$	11.27	12.44	5.56 (9.15) <sup>a</sup>	6.66 (9.85) <sup>a</sup>	-25.76	-24.35
13b.	(RR)	$\text{CH}_3\text{COHCH}_3 + \text{H} \rightarrow \text{CH}_3\text{CHOHCH}_3$	...	...	0.00	0.00	-90.73	-91.08
14a.	(NR)	$\text{CH}_3\text{COCH}_3 + \text{H} \rightarrow \text{CH}_3\text{CHOCH}_3$	12.97	12.97	6.29	6.55 (—) <sup>b</sup>	-16.40	-24.35
14b.	(RR)	$\text{CH}_3\text{CHOCH}_3 + \text{H} \rightarrow \text{CH}_3\text{CHOHCH}_3$	...	...	0.00	0.00	-100.10	-91.08
Ethenone - Vinyl alcohol								
15a.	(NR)	$\text{CH}_2\text{CO} + \text{H} \rightarrow \text{CH}_2\text{COH}$	17.52	18.22	11.80 (5.39)	12.49 (17.59) <sup>a</sup>	-15.60	-16.96
15b.	(RR)	$\text{CH}_2\text{COH} + \text{H} \rightarrow \text{CH}_2\text{CHOH}$	...	...	0.00	0.00	-45.67	-45.30
16a.	(NR)	$\text{CH}_2\text{CO} + \text{H} \rightarrow \text{CH}_2\text{CHO}$	10.04	9.92	4.36 (3.97)	4.26 (5.43) <sup>a</sup>	-41.76	-43.87
16b.	(RR)	$\text{CH}_2\text{CHO} + \text{H} \rightarrow \text{CH}_2\text{CHOH}$	...	...	0.00	0.00	-19.51	-18.40

NOTE— NR refers to Neutral-Radical reactions, and RR to Radical-Radical reactions.

<sup>a</sup>Bracketed values are calculated using CCSD(T)/aug-cc-pVTZ level, <sup>b</sup>We did not find true transition state, <sup>i</sup>Song & Kästner (2017), <sup>ii</sup>Zaverkin et al. (2018), <sup>iii</sup>Álvarez-Barcia et al. (2018).

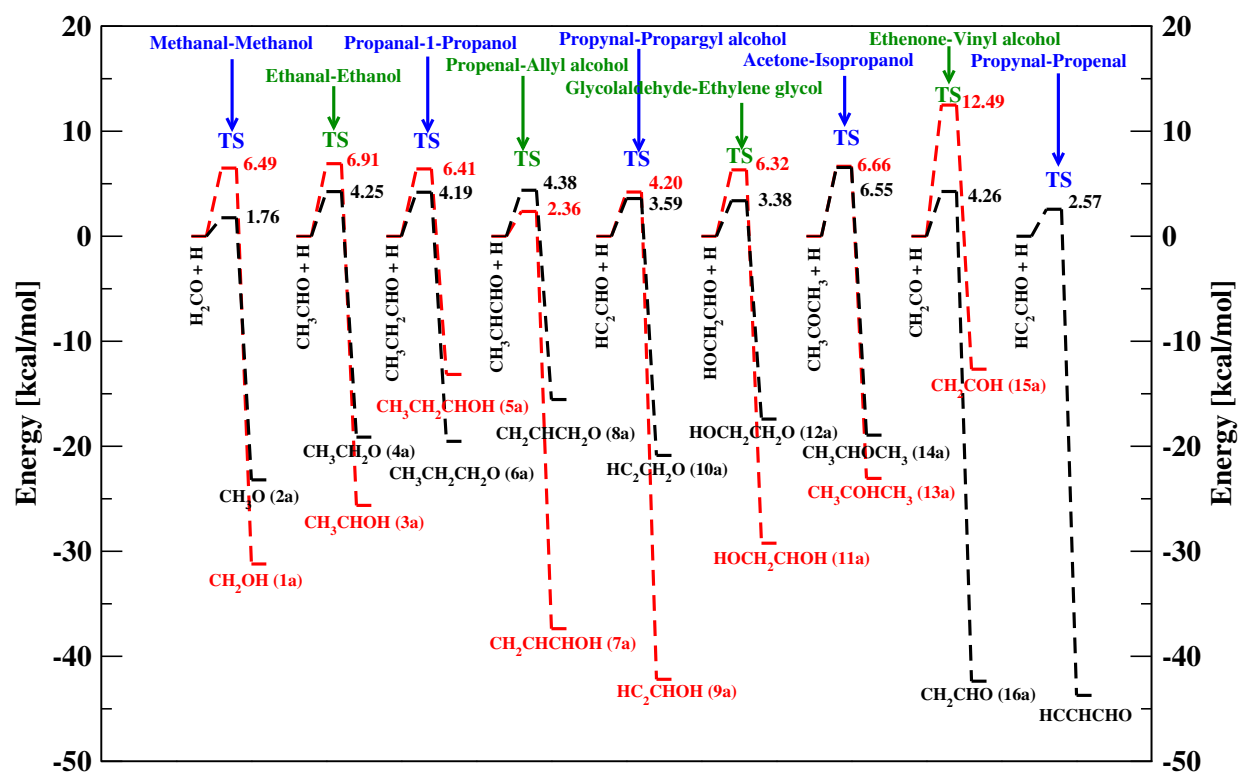


**Figure 2.** Schematic potential energy surfaces of alcohol formation from aldehyde and ketone for various hydrogenation reactions (representing IEFPCM correction for the influence of ice) indicating stable species and transition states. Energy differences in units of kcal/mol are shown, referenced to reactant complexes calculated using DFT-B3LYP/6-31G+(d,p) level of theory. The red lines denote H addition at O positions, whereas the black lines represent H addition at C positions.

High-level quantum chemical calculations of six aldehyde-alcohol pairs with one ketone-alcohol and one ketene-alcohol pairs are presented and discussed in detail. Aldehyde to alcohol, ketone to alcohol, ketene to alcohol formation may occur through successive hydrogen addition reaction in two steps: The first step is aldehyde/ketone/ketene + H  $\rightarrow$  radical-1 and the second step is radical-1 + H  $\rightarrow$  alcohol. The first step of all these reactions is neutral-radical reactions, whereas the second step is a radical-radical reaction. The first step of all these reactions thus having an activation barrier, whereas the second step is barrierless as both reactants have free electrons, which makes them very reactive. Our calculations show that six aldehydes (such as methanal, ethanal, propanal, propenal, propynal, and glycolaldehyde), one ketone (such as acetone), and one ketene (such as ethenone) are forming alcohols (such as methanol, ethanol, 1-propanol, allyl alcohol, propargyl alcohol, ethylene glycol, isopropanol, and vinyl alcohol, respectively) via two successive hydrogen addition reactions. In terms of stability, the observed alcohols are thermodynamically favorable compared to their isomers. The formation of complex molecules on the grain surface through successive hydrogen additions is found to be dominant. Formation pathways of these molecules are discussed below, and a graphical representation of PESs of their formation mechanism considering IEFPCM model and DFT-B3LYP/6-31G+(d,p) level of theory is shown in Figure 2.

### 3.1.1. Methanal and Methanol

Here, the activation barrier of the reaction H + H<sub>2</sub>CO is computed, for the production of CH<sub>2</sub>OH or CH<sub>3</sub>O (reactions 1a and 2a of Table 3). It is noticed that the hydrogen addition to the carbon atom of H<sub>2</sub>CO (i.e., the formation of CH<sub>3</sub>O, methoxy radical) is more favorable than that of its addition to the O atom of H<sub>2</sub>CO (i.e., the formation of CH<sub>2</sub>OH) in both gas- and ice-phases considering both (DFT-B3LYP/6-31+G(d,p) and CCSD(T)/aug-cc-pVTZ) level of theory. This is consistent with earlier experimental and theoretical results (Chuang et al. 2016; Song & Kästner 2017). Song & Kästner (2017) studied the TS of reactions 1a and 2a both in gas-phase and on five different binding sites of the amorphous solid water (ASW) surface and calculated the corresponding activation energies. We compare our activation energy values with their gas-phase and ice-phase for binding site ASW 5 in Table 3, which shows a good agreement when we considered CCSD(T)/aug-cc-pVTZ level of theory. Woon (2002a) predicted the barrier height of reaction 2a as 5.04 kcal/mol for the gas-phase and it decreases to 4.81 kcal/mol when the reaction is embedded with the IPCM field. In our case, we also found the similar decreasing trend from gas-phase to ice-phase considering both level of theory. Song & Kästner (2017) also computed the BE of H<sub>2</sub>CO for different sites of amorphous solid water (ASW) surface and found that BE val-

ues vary between 1000 K and 9370 K. This uncertainty in the BE value may lead to a very different abundance of CH<sub>3</sub>OH under different astrophysical environments. The hydrogen abstraction reaction of methanol also plays an essential role in controlling the abundance of COMs. Methanol abstraction reaction barrier and the rate constant are taken from Song & Kästner (2017).

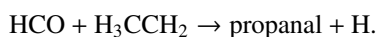
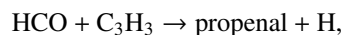
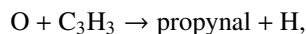
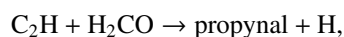
### 3.1.2. Ethanal and Ethanol

Here, the formation of C<sub>2</sub>H<sub>5</sub>OH via two successive hydrogen addition reactions with the CH<sub>3</sub>CHO is considered. Kinetic information (i.e., activation barrier and reaction enthalpy) of these two reactions are noted in Table 3. Looking at the activation barriers reported in Table 3, it is clear that similar to methanol formation, here also, the hydrogen addition at the carbon atom position of CH<sub>3</sub>CHO (i.e., the formation of CH<sub>3</sub>CH<sub>2</sub>O, reaction 4a) is more efficient compared to the hydrogen addition at the O atom position (i.e., the formation of CH<sub>3</sub>CHOH, reaction 3a). The relative abundances between the acetaldehyde and ethyl alcohol seem to depend upon the evolution time, availability of the hydrogen atoms, ice thickness, and ice morphology (Bisschop et al. 2007, 2008). Only the hydrogenation reactions are not enough in explaining the observed abundances of ethanal-ethanol. It is needed to consider the ice phase reaction between CH<sub>3</sub> and CH<sub>2</sub>OH for the formation of ethanol in the ice phase.

### 3.1.3. Propanal and 1-Propanol

The coexistence of propanal, propynal, and propenal in Sgr B2(N) (Hollis et al. 2004) could be explained by the following successive hydrogenation sequences; HC<sub>2</sub>CHO (propynal)  $\rightarrow$  CH<sub>2</sub>CHCHO (propenal)  $\rightarrow$  CH<sub>3</sub>CH<sub>2</sub>CHO (propanal). Recently, Qasim et al. (2019) studied the propanal formation by the radical-radical reaction between HCO and H<sub>3</sub>CCH<sub>2</sub>. They used the sequential hydrogenation of propanal to form 1-propanol. The first step of the reaction has a high activation barrier. But this reaction can change the saturated bond to the unsaturated radicals, which may again undergo some radical-radical recombination reactions. Qasim et al. (2019) obtained a significant production of 1-propanol with this pathway. Our TST calculation for the successive hydrogenation pathways is shown in Table 3. It is noticed that the hydrogen addition at the carbon atom position of propanal (CH<sub>3</sub>CH<sub>2</sub>CH<sub>2</sub>O formation, reaction 6a of Table 3) is favorable compared to the oxygen atom position of propanal (CH<sub>3</sub>CH<sub>2</sub>CHOH formation, reaction 5a). The gas-phase activation and reaction energies (including ZPVE) of Zaverkin et al. (2018) are compared with ours in Table 3 which is in good agreement with our values calculated using higher-level of theory. Except the successive hydrogenation reactions, following ice phase reactions, are also considered

for the formation of propynal, propenal, and propanal.



### 3.1.4. Propenal and Allyl Alcohol

Propenal is also a product of the two successive hydrogenation reactions with propynal.



Here, the other product channel of this reaction is studied. Firstly, the hydrogenation reaction of propynal would form propenal. In the second step, propenal could undergo another hydrogenation reaction to form allyl alcohol. The TS calculation of the first step found an activation barrier of 2.60 kcal/mol in the gas phase and 2.57 kcal/mol in the ice phase considering lower-level of theory (see Figure 2). Table 3 shows the activation barriers for the hydrogen addition at the propenal's carbon and oxygen atom position. It is noted that, unlike the other cases, here, the hydrogen addition at the oxygen atom of propenal ( $\text{CH}_2\text{CHCHOH}$  formation, reaction 7a) seems to be more favorable than it is with the carbon atom position ( $\text{CH}_2\text{CHCH}_2\text{O}$  formation, reaction 8a) considering lower-level of theory. But considering higher-level of theory, opposite trend is found which agrees well with the values calculated by Zaverkin et al. (2018) shown in Table 3 for comparison.

### 3.1.5. Propynal and Propargyl Alcohol

Transformation from propynal ( $\text{HC}_2\text{CHO}$ ) to propargyl alcohol was already reported by Gorai et al. (2017b). This happened via two successive hydrogenations with propynal :

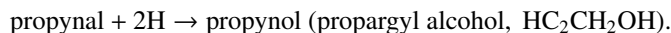


Table 3 shows a different trend for the hydrogen addition for reactions 9a and 10a in the gas-phase. The hydrogen addition to the oxygen atom position (reaction 9a) is favorable than that of the carbon atom position (reaction 10a) using lower-level of theory, whereas Zaverkin et al. (2018) found an opposite trend. In contrast, the opposite trend is noticed for the ice-phase using both lower- and higher-level of theory.

### 3.1.6. Glycolaldehyde and Ethylene Glycol

Glycolaldehyde is the simplest form of the aldose family. The sugars like glucose, ribose, and erythrose belong to this family. Therefore, the presence of glycolaldehyde in

space is an indication of the precursor of biologically relevant molecules. Identification of the numerous complex organic molecules in the Galactic Centre (GC) makes it an active area of research. Specifically, the study of the chemical evolution of the grain mantle, where various energetic processes (like UV radiation, X-rays, and cosmic rays, etc.) may reprocess the mantle composition, are fascinating. The C and O addition to the formyl radical and then three successive hydrogen additions yield glycolaldehyde. The two subsequent hydrogen additions to the glycolaldehyde can produce ethylene glycol (Charnley 2001). Fedoseev et al. (2015) proposed that two HCO radicals can recombine to produce glyoxal ( $\text{HC(O)CHO}$ ), which can also subsequently convert to glycolaldehyde. Coutens et al. (2018) investigated the formation mechanism of these two species (glycolaldehyde and ethylene glycol) using a gas-grain chemical model. They studied the EG/GA ratio for various luminosities. Álvarez-Barcia et al. (2018) studied two successive hydrogen addition reactions with acetaldehyde which can produce ethylene glycol. They also studied the hydrogen abstraction reactions of GA and EG. Table 3 shows the kinetics involved in converting ethylene glycol from glycolaldehyde. Like the methanal-methanol, ethanal-ethanol, propanal-1-propanol, and ice phase pathways of propynal-propargyl alcohol pairs, the favorable position of the hydrogen addition is noted to be the carbon atom ( $\text{HOCH}_2\text{CH}_2\text{O}$  formation, reaction 12a) instead of the oxygen atom ( $\text{HOCH}_2\text{CHOH}$  formation, reaction 11a) of glycolaldehyde.

### 3.1.7. Acetone and Isopropanol

Acetone ( $\text{CH}_3\text{COCH}_3$ , propanone) and isopropanol ( $\text{CH}_3\text{CHOHCH}_3$ , isopropyl alcohol, 2-propanol) might be chemically connected. Table 3 shows the two successive hydrogenations of acetone (reactions 13 and 14). We check the TST calculations for the hydrogen addition either with the oxygen atom (activation energy 5.56 kcal/mol) or with the carbon atom (activation energy 6.29 kcal/mol) position of acetone and found that the former one is more favorable than the latter in the gas phase considering lower-level of theory. In contrast, the opposite trend was noted in the ice phase. We could not find a proper TS using higher-level of theory for reaction 14a in the ice-phase.

### 3.1.8. Ethenone and Vinyl Alcohol

Vinyl alcohol is a planar molecule, which has two conformations. The "syn" conformer is found to be more stable than that of the "anti" conformer (Turner & Apponi 2001). Here also, the "syn" conformer of vinyl alcohol is considered for the quantum chemical calculations. Here, the TS of the two successive hydrogen addition reactions to ketene is examined for the formation of vinyl alcohol. The first step has an activation barrier, whereas the second step is a radical-radical reaction and is assumed to be barrierless. Vinyl al-

cohol can also form from acetaldehyde via the isomerization process (Käser et al. 2020). Table 3 depicts that the hydrogen addition at the carbon atom position is more favorable than the oxygen atom position of ethenone. Table 3 shows that the H addition to the O atom position of ketene (reaction 15a) requires a significantly higher activation barrier than the H addition to the O atom position of the other species (reactions 1a, 3a, 5a, 7a, 9a, 11a, 13a) reported here. It could be due to the change of the hybridization of C atom of ketene from  $sp$  (linear) to  $sp^2$  (bent) during the H addition reaction. On the other hand, there is no change of hybridization upon H addition to the other aldehyde, which requires only small structural change and thus, the activation energy could be small. Carr et al. (1968) studied the reaction of ketene with atomic H at room temperature where the reaction  $H + H_2CCO \rightarrow CH_3CO^* \rightarrow CH_3 + CO$  occurs rather slowly (rate constant  $1.3 \times 10^{-13} \text{ cm}^3 \text{ mol}^{-1} \text{ s}^{-1}$ ), while neither  $H + H_2CCO \rightarrow CH_2CHO$  nor H abstraction occur very significantly.

### 3.2. Binding Energy and Proton Affinity

A sizable portion ( $\sim 60 - 70\%$  of the surface coverage) of the interstellar icy layers may contain water molecules. That is why the BE of the interstellar species is usually explored with the  $H_2O$  surface. However, the rest ( $\sim 30 - 40\%$ ) of the grain mantle would comprise other impurities.  $CO_2$ ,  $CO$ , and  $CH_3OH$  can occupy a sizable portion of the grain mantle in different lines of sight. Keane et al. (2001) summarized the relative abundance of  $CO$ ,  $CO_2$ , and  $CH_3OH$  relative to water ice could vary in the range of  $0.4 - 15$ ,  $0.17 - 21$ , and  $1.5 - 30$ , respectively, in different lines of sight. So, the BE with these surface species is also important in the various evolutionary phases. It is needed to construct a model which can consider the BE depending on the surface composition of the ice. Furuya & Persson (2018) reported a model in which the BE depends on the surface composition of ice mantles. However, showing the results of such a chemical model is out of scope for this work.

A realistic estimation of the BEs with various substrates is not available. In the absence of any experimental values, the quantum chemical method provides an educated estimate (Das et al. 2018; Wakelam et al. 2017). Here,  $CO$  and  $CH_3OH$  molecules are considered a substrate for this purpose.

Gaussian 09 suite of programs employed for the quantum chemical calculations is utilized to evaluate the BE values. To calculate the BE, which is opposite to interaction energy for the bound system, the optimized energy for the complex system (where a species is placed at a suitable distance from the grain surface) is subtracted from the total optimized energies of the grain surface and species. To find the optimized energy of all structures, a Second-order Møller-

Plesset (MP2) method with an aug-cc-pVDZ basis set (Dunning 1989) is used following Das et al. (2018). The ZPVE and basis set superposition error (BSSE) correction are not considered for BE calculations.

Obtained BE values are shown in Table 4. It is interesting to note that a higher BE for the alcohol is obtained in most cases than their corresponding aldehyde, ketone, or ketene. Obtained values with  $CO$  and  $CH_3OH$  significantly differ from that of water. In terms of average values, the BE values with water monomer is  $\sim 2.85$  times higher than the  $CO$  monomer and  $1.16$  times lower in comparison to  $CH_3OH$  monomer. Here, in our chemical model, the obtained BE values with  $CO$  and  $CH_3OH$  are not included because it is not available for the other species. However, BE values obtained with the c-tetramer water configuration are included in our model with an appropriate scaling factor suggested in Das et al. (2018). In Table 4, the ground state spin multiplicity of the species used to calculate the BE is also noted. Separate calculations (job type “opt+freq” in Gaussian 09 suite) with different spin multiplicities are used. The lowest energy electronic state in between these is noted as the ground state.

The protonation reactions (i.e.,  $X + H^+ \rightarrow XH^+$ ) and proton transfer reactions (i.e.,  $X + YH^+ \rightarrow XH^+ + Y$ ) have a significant impact on the interstellar chemistry (Wakelam et al. 2010; Herbst & Leung 1986). The ab-initio quantum chemical approaches provide a reliable value of the proton affinity for small molecules where the experimental determination of these parameters is a difficult task. A systematic study to calculate the adiabatic PA of aldehydes, ketone, ketene, and corresponding alcohols is considered in this work. PA is defined as the energy released when a proton is added to a system. Thus the energy difference between a species and a species with an additional proton ( $H^+$ ) is estimated. It is calculated as the difference in energy (electronic + zero-point energy) between a neutral species and its protonated analog, i.e.,

$$PA = E_X - E_{XH^+}, \quad (6)$$

where  $E_X$  is the optimized energy of the species  $X$ , and  $E_{XH^+}$  is the optimized energy of the protonated species,  $XH^+$ . To find the optimized energy of all structures, a Second-order Møller-Plesset (MP2) method with an aug-cc-pVDZ basis set is again used. This is then verified via harmonic frequency calculations with the equilibrium geometries having only real frequencies. Zero-point correction to energies is not considered to evaluate the PA of the species reported here. The protonation of a neutral species can occur in more than one position, which yields different protonated species with other PA. To avoid any ambiguity, only the highest PA is noted in Table 5. Protonated form with higher PA of a neutral species is found to be more stable and more abundant (in some cases), and thus may be detectable. In contrast, another protonated form with lower PA forming from the same neutral species

**Table 4.** Calculated binding energy values of the aldehydes, alcohols, ketone and ketene considered in this work.

Species	Ground state	Binding Energy (Kelvin)				
		used	CO monomer	CH <sub>3</sub> OH monomer	H <sub>2</sub> O monomer	H <sub>2</sub> O tetramer (scaled by 1.188)
Methanal	Singlet	641	2942	2896	3242 <sup>a</sup> (3851)	2050 <sup>b</sup> , 4500 ± 1350 <sup>c</sup>
Methanol	Singlet	1247	3227	3124	4368 <sup>a</sup> (5189)	5534 <sup>b</sup> , 5000 ± 1500 <sup>c</sup>
Ethanal	Singlet	1015	1964	3189	3849 <sup>a</sup> (4573)	2450 <sup>b</sup> , 5400 ± 1620 <sup>c</sup>
Ethanol	Singlet	873	3408	2824	5045 (5993)	6584 <sup>b</sup> , 5400 ± 1620 <sup>c</sup>
Propanal	Singlet	680	3679	3522	3396 (4034)	4500 ± 1350 <sup>c</sup>
1-Propanol	Singlet	1298	3932	2609	4791 (5692)	...
Propenal	Singlet	1043	3236	3170	3495 (4152)	5400 ± 1620 <sup>c</sup>
Allyl Alcohol	Singlet	1381	3625	2958	5964 (7085)	...
Propynal	Singlet	1174	3072	2318	3379 (4014)	...
Propargyl Alcohol	Singlet	1031	4119	2870	4284 (5089)	...
Glycolaldehyde	Singlet	826	3254	2871	5131 (6096)	...
Ethylene Glycol	Singlet	933	4666	3144	4602 (5467)	...
Acetone	Singlet	728	3769	3623	4420 (5251)	3500 <sup>b</sup>
Isopropanol	Singlet	1369	3640	2879	5230 (6213)	...
Ethenone	Singlet	732	1450	1317	2847 (3382)	2200 <sup>b</sup> , 2800 ± 840 <sup>c</sup>
Vinyl Alcohol	Singlet	1236	3407	2836	3786 (4497)	...

NOTE—<sup>a</sup>Das et al. (2018), <sup>b</sup>KIDA old BE, <sup>c</sup>KIDA new BE (Wakelam et al. 2017).

**Table 5.** Calculated proton affinity of these species.

Species	Protonation Reactions	Proton Affinity (kJ/mol)	
		Our calculation	Available
Methanal	HCHO + H <sup>+</sup> → CH <sub>2</sub> OH <sup>+</sup>	692	712.9 ± 1.1 <sup>a</sup>
Methanol	CH <sub>3</sub> OH + H <sup>+</sup> → CH <sub>3</sub> OH <sub>2</sub> <sup>+</sup>	740	754.3 <sup>a</sup>
Ethanal	CH <sub>3</sub> CHO + H <sup>+</sup> → CH <sub>3</sub> CHOH <sup>+</sup>	749	768.5 ± 1.6 <sup>a</sup>
Ethanol	C <sub>2</sub> H <sub>5</sub> OH + H <sup>+</sup> → C <sub>2</sub> H <sub>5</sub> OH <sub>2</sub> <sup>+</sup>	764	
Propanal	CH <sub>3</sub> CH <sub>2</sub> CHO + H <sup>+</sup> → HCH <sub>3</sub> CH <sub>2</sub> CHO <sup>+</sup>	769	
1-Propanol	CH <sub>3</sub> CH <sub>2</sub> CH <sub>2</sub> OH + H <sup>+</sup> → HCH <sub>3</sub> CH <sub>2</sub> CH <sub>2</sub> OH <sup>+</sup>	770	
Propenal	CH <sub>2</sub> CHCHO + H <sup>+</sup> → CH <sub>2</sub> CHCHOH <sup>+</sup>	764	
Allyl Alcohol	CH <sub>2</sub> CHCH <sub>2</sub> OH + H <sup>+</sup> → CH <sub>2</sub> CHCH <sub>2</sub> OH <sub>2</sub> <sup>+</sup>	773	
Propynal	HC <sub>2</sub> CHO + H <sup>+</sup> → HC <sub>2</sub> CHOH <sup>+</sup>	733	
Propargyl Alcohol	HC <sub>2</sub> CH <sub>2</sub> OH + H <sup>+</sup> → HC <sub>2</sub> CH <sub>2</sub> OH <sub>2</sub> <sup>+</sup>	742	
Glycolaldehyde	HOCH <sub>2</sub> CHO + H <sup>+</sup> → H <sub>2</sub> OCH <sub>2</sub> CHO <sup>+</sup>	759	
Ethylene Glycol	HOCH <sub>2</sub> CH <sub>2</sub> OH + H <sup>+</sup> → HOCH <sub>2</sub> CH <sub>2</sub> OH <sub>2</sub> <sup>+</sup>	797	
Acetone	CH <sub>3</sub> COCH <sub>3</sub> + H <sup>+</sup> → CH <sub>3</sub> COHCH <sub>3</sub> <sup>+</sup>	793	
Isopropanol	CH <sub>3</sub> CHOHCH <sub>3</sub> + H <sup>+</sup> → CH <sub>3</sub> CHOH <sub>2</sub> CH <sub>3</sub> <sup>+</sup>	782	
Ethenone	CH <sub>2</sub> CO + H <sup>+</sup> → CH <sub>3</sub> CO <sup>+</sup>	822	825.3 ± 3 <sup>a</sup>
Vinyl Alcohol	CH <sub>2</sub> CHOH + H <sup>+</sup> → CH <sub>3</sub> CHOH <sup>+</sup>	800	882.8 <sup>b</sup>

NOTE—<sup>a</sup>Hunter & Lias (1998), <sup>b</sup>Turner & Apponi (2001)

is less stable. This species is very reactive, and the high reactivity of this protonated species may reduce its interstellar abundance. We notice that ethenone has the highest and methanal has the lowest PA among all the species considered for this study.

#### 4. CHEMICAL MODELING

The Chemical Model for Molecular Cloud (hereafter CMMC) (Das et al. 2015a,b; Das et al. 2019, 2021; Gorai

et al. 2017a,b; Sil et al. 2018; Bhat et al. 2021; Gorai et al. 2020; Sil et al. 2021) is implemented for studying the formation of aldehydes, ketone, ketene and their corresponding alcohols. The low metallic elemental abundances are used as the initial abundances (Wakelam & Herbst 2008, EA1 set). Gas-phase pathways of CMMC are mainly adopted from the UMIST database (McElroy et al. 2013). Additionally, a complete network for the formation of alcohols and aldehydes is considered. For the construction of these reaction sets, the

**Table 6.** Comparison between the observed abundance and our CMMC results with Model C (set 4).

Species	Obtained abundances	Obtained abundance	Observed abundances			
	from model	ratio from model	G31.41+0.31	Sgr B2 (N)	Orion KL	G10.47+0.03
Methanal	3.3(-9) – 5.8(-7)		[1.9(-7)] <sup>e</sup>	[3.2(-08)] <sup>m</sup>		[6.1(-7)] <sup>b</sup>
Methanol	3.5(-8) – 1.4(-5)	1.0(1) – 5.3(1)	[1.9(-6)] <sup>e</sup>	[7.7(-7)] <sup>m</sup> [7.1(-6)] <sup>x</sup>	[2.2(-7)] <sup>l</sup>	[3.2 ± 2.5(-7)] <sup>a</sup> , [1.8(-6)] <sup>b</sup>
Ethanal	1.8(-13) – 5.0(-9)		[1.0(-9)] <sup>n</sup>	[1.4(-08)] <sup>m</sup> [9.5(-8)] <sup>x</sup>		[5.0 ± 0.8(-10)] <sup>a</sup>
Ethanol	7.4(-10) – 9.7(-8)	8.0(-2) – 2.6(4)	[2.0(-8)] <sup>n</sup> [1.3(-9)] <sup>f</sup>	[1.1(-7)] <sup>m</sup> [3.6(-7)] <sup>x</sup>	[1.3(-8)] <sup>l</sup>	[1.2(-7)] <sup>b</sup>
Propanal	7.3(-10) – 4.8(-8)					[1.8 ± 0.2(-8)] <sup>a</sup>
1-Propanol	2.4(-12) – 1.1(-7)	2.6(-4) – 1.3(2)				
Propenal	2.0(-13) – 1.9(-9)					[1.2(-10)] <sup>a,d</sup>
Allyl alcohol	8.7(-15) – 1.7(-9)	3.6(-2) – 2.9(0)				
Propynal	3.1(-11) – 2.2(-09)					
Propargyl alcohol	6.4(-15) – 1.3(-11)	1.4(-4) – 1.0(-2)				
Glycolaldehyde	2.8(-15) – 1.3(-06)		[8.3(-11)] <sup>f</sup>	[3.2(-10)] <sup>m</sup> [1.9(-8)] <sup>x</sup>	[1.5(-10)] <sup>l</sup>	[9.6 ± 0.007(-10)] <sup>a</sup>
Ethylene glycol	5.5(-17) – 1.6(-5)	1.9(-2) – 4.45(2)	[1.7(-10)] <sup>f</sup>	4.1(-10)] <sup>m</sup>	[2.3(-9)] <sup>l</sup>	[3.7 ± 1.5(-8)] <sup>a</sup>
Acetone	6.6(-14) – 1.7(-8)			[2.6(-8)] <sup>m</sup>		[4.0 ± 0.5(-8)] <sup>a</sup> , [1.0(-7)] <sup>b</sup>
Isopropanol	1.2(-13) – 4.4(-9)	9.7(-2) – 7.4(3)				
Ethenone	4.6(-13) – 5.5(-9)					[8.0(-8)] <sup>b</sup>
Vinyl alcohol	3.5(-11) – 1.4(-8)	1.9(0) – 7.7(1)				[≤2.3(-9)] <sup>a,d</sup>
Methyl formate	2.3(-11) – 1.3(-6)		[2.6(-9)] <sup>f</sup>	[7.7(-8)] <sup>m</sup> [9.5(-8)] <sup>x</sup>	[1.2(-7)] <sup>k</sup>	[6.7 ± 0.5(-8)] <sup>a</sup> , [1.4(-7)] <sup>b</sup>
Dimethyl ether	3.5(-9) – 1.5(-7)	1.2(-1) – 1.5(2)	[4.2(-9)] <sup>f</sup>	[3.5(-7)] <sup>m</sup>	[3.0(-7)] <sup>k</sup>	[1.1 ± 0.3(-8)] <sup>a</sup> , [3.0(-7)] <sup>b</sup>

NOTE—

<sup>a</sup>G31 observation: <sup>e</sup> Gorai et al. (2021) (used ALMA with  $\theta_b = 0.98'' - 1.19''$  and  $N_{\text{H}_2} = 1.53 \times 10^{25} \text{ cm}^{-2}$ ), <sup>f</sup> Rivilla et al. (2017) (used SMA with  $\theta_b = 0.75'' - 3.5''$  and  $N_{\text{H}_2} = 1.2 \times 10^{26} \text{ cm}^{-2}$ ), <sup>n</sup> Nummelin et al. (1998) (used SEST and IRAM with  $\theta_b = 10''$  and  $N_{\text{H}_2} = 1.6 \times 10^{23} \text{ cm}^{-2}$ )  
Sgr B2 observation: <sup>x</sup> Belloche et al. (2014) (used ALMA with  $\theta_b = 1.2'' - 1.9''$  and  $N_{\text{H}_2} = 5.6 \times 10^{24} \text{ cm}^{-2}$ ), <sup>m</sup> Belloche et al. (2013) (used IRAM with  $\theta_b = 10'' - 25''$  and  $N_{\text{H}_2} = 5.6 \times 10^{24} \text{ cm}^{-2}$ ) (Belloche et al. 2014)  
Orion KL observation: <sup>l</sup> Brouillet et al. (2015) (used ALMA with  $1.4'' - 1.9''$  and  $N_{\text{H}_2} = 2.0 \times 10^{24} \text{ cm}^{-2}$  (Favre et al. 2011)), <sup>k</sup> Tercero et al. (2015) (used ALMA with  $1.29'' - 2''$  and  $N_{\text{H}_2} = 2.0 \times 10^{24} \text{ cm}^{-2}$  (Favre et al. 2011))  
G10 observation: <sup>a</sup> This work (used ALMA with  $\theta_b = 1.39'' - 2.44''$  and  $N_{\text{H}_2} = 1.35 \times 10^{25} \text{ cm}^{-2}$ ), <sup>b</sup> Rolffs et al. (2011) (used SMA with  $\theta_b = 0.28'' - 4.27''$  and with  $N_{\text{H}_2} = 5 \times 10^{24} \text{ cm}^{-2}$ ), <sup>d</sup> Dickens et al. (2001) (used SEST & NRAO for possible detection of propenal and upper limit for vinyl alcohol with  $\theta_b = 45''$  and  $N_{\text{H}_2} = 10^{23} \text{ cm}^{-2}$ )

a

ice phase reactions noted in Table 3 are considered. The activation energy barriers calculated with the CCSD(T)/aug-cc-pVTZ level are adopted. Since, for the reaction 13a of Table 3, a true TS was not obtained with the CCSD(T)/aug-cc-pVTZ level of theory, the activation barrier obtained with the B3LYP/6-31+G(d,p) level of theory is used. For the gas phase destruction of these species, interstellar photoreactions, cosmic-ray induced reactions, and ion-molecular reactions with major ions ( $\text{He}^+$ ,  $\text{H}_3^+$ ,  $\text{HCO}^+$ ,  $\text{H}_3\text{O}^+$ ,  $\text{C}^+$ , etc.) are considered. The destruction of some of these reactions was already available in McElroy et al. (2013). If it is not available, a very similar reaction with the same rate constants is adopted for these reactions. A cosmic ray rate of  $1.3 \times 10^{-17} \text{ s}^{-1}$  is considered in all our models. Cosmic ray-induced desorption and chemical desorption with the efficiency of 1% is considered. For the all-grain surface species, a photodesorption rate of  $3 \times 10^{-3}$  per incident UV photon (Öberg et al. 2007) is adopted. A sticking coefficient of 1.0 is considered for the neutral species. Sticking coefficients of H and  $\text{H}_2$  is taken from Chaabouni et al. (2012). On the grain surface,

the diffusive surface reaction can lead to chemical complexity. However, to successfully continue the diffusive reaction mechanism, the reactants should be in the close vicinity until they react. There is a possibility that two reactants can move apart or be desorbed back to the gas phase. So it is essential to consider the competition between diffusion, desorption, and reaction. Following Garrod & Pauly (2011), here this possibility is included. At the high density ( $\sim 10^7 \text{ cm}^{-3}$ ) and around 10 K, a notable portion of the grain surface would be covered by molecular hydrogen. At this stage, encounter desorption of  $\text{H}_2$  (Hincelin et al. 2015; Chang et al. 2021; Das et al. 2021) needs to be considered to avoid an unnecessary surge in the grain's molecular hydrogen. The grain mantle's chemical composition at this phase is crucial to delivering the surface species into the gas phase during the warm-up stage. Here, the encounter desorption mechanism of  $\text{H}_2$  is considered in our model.

The BE ( $E_d$ ) of the surface species plays a decisive role in controlling the chemical complexity of the interstellar ice. A straightforward relation between the diffusion energy ( $E_b$ ) of

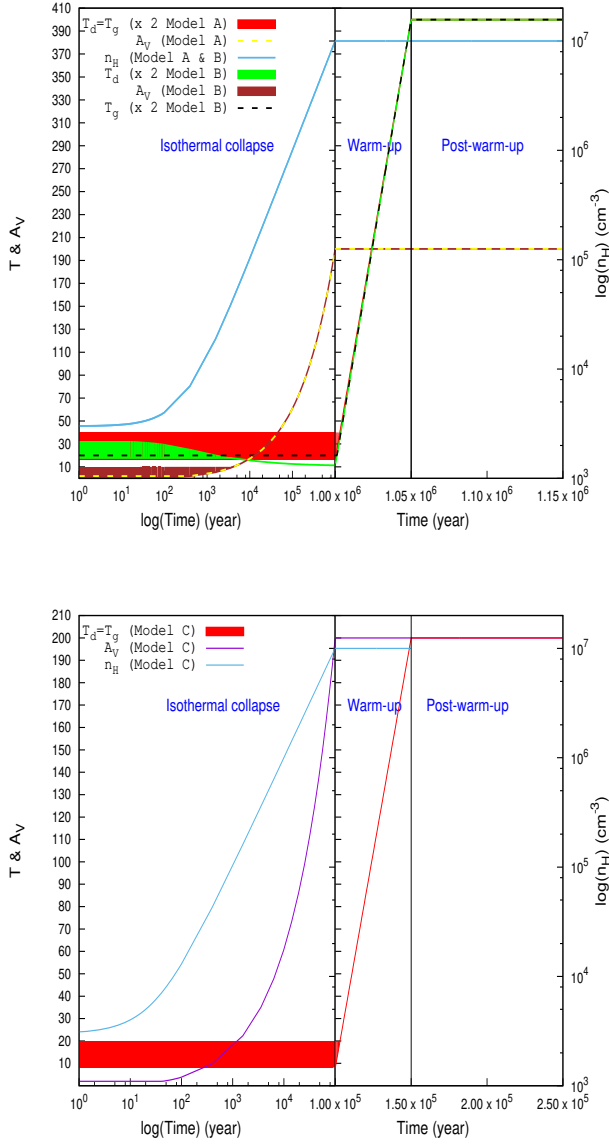


**Figure 3.** Physical conditions considered in Model A and Model B are shown in the upper panel and in the lower panel, we show the adopted physical conditions for Model C. The X-axis of the figure shows the logarithmic scale for the isothermal collapsing phase, whereas, beyond that, it is shown on the regular scale. In case of Model A and Model C, an isothermal collapsing phase is considered whereas in Model B, a pre-stellar core phase is considered where temperature is decreased in the upper panel, temperature is scaled by a factor of 2 for the better visibility.

**Table 7.** Different sets of BE used based on the ratio between the diffusion energy to binding energy ( $R$ ).

	BEs used	$R$
set 1	Wakelam et al. (2017)	0.5
set 2	Wakelam et al. (2017)	0.35
set 3	$1.188 \times$ BE of Das et al. (2018)	0.35
set 4	$1.188 \times$ BE of Das et al. (2018), BE of H, and H <sub>2</sub> from Wakelam et al. (2017)	0.35

816 the KIDA database<sup>3</sup> or taken from Das et al. (2018). Das  
 817 et al. (2018) provided BE values for some relevant interstellar  
 818 species with the water surface. They computed the interaction  
 819 energies, varying the size of the substrate. They showed  
 820 that their method would yield a minimum deviation with the  
 821 experimentally obtained BE values when a higher-order cluster  
 822 is used. Table 4 shows the computed BEs of these aldehydes,  
 823 alcohols, ketone, and ketene with various substrates. The ground  
 824 state used to calculate the BE of these molecules is also pointed  
 825 out along with the BE values in Table 4. Das et al. (2018)  
 826 suggested a scaling factor  $\sim 1.188$  while using the tetramer  
 827 water configuration for the computation of the BE. The scaled  
 828 BE values are also noted in Table 4. Except for the glycolaldehyde  
 829 and ethylene glycol pair, for all the cases, obtained BEs with  
 830 the tetramer configuration are noted to be comparatively higher  
 831 than that of their related aldehyde, ketone, or ketene. These  
 832 new sets of BEs with the tetramer configuration of water  
 833 molecules are included in our chemical model with appropriate  
 834 scaling.

835 Depending on the BEs and  $R$  values, four sets of BEs are  
 836 constructed (see Table 7). For set 1 and set 2, BEs are used  
 837 from the KIDA database (Wakelam et al. 2017). The only  
 838 difference between set 1 and set 2 is that for set 1,  $R = 0.5$   
 839 is used, whereas, for set 2,  $R = 0.35$  is used. Recently, Das  
 840 et al. (2018) provided a set of BEs for 100 relevant interstellar  
 841 species with the water surface. They used the tetramer  
 842 configuration of water molecules for this calculation. They  
 843 suggested using a scaling factor of 1.188 with this to estimate  
 844 the BEs of these species. The set 3 is constructed with the  
 845 BE values provided by Das et al. (2018). Sil et al. (2017)  
 846 reported the BEs of H and H<sub>2</sub> for a comprehensive collection  
 847 of surfaces (benzene, silica, and water). They showed that the  
 848 BE of H and H<sub>2</sub> are very sensitive to the choice of substrates.  
 849 These variations should be expected for all the species if  
 850 various substrates would have been considered. But showing all  
 851 the changes here would be out of scope for this work. Here,  
 852 one additional BE set is considered, where the BE of H and  
 853 H<sub>2</sub> are kept the same as it was used in KIDA, but for the  
 854 others, it is the same as it is in set 3. Thus, in set 3, BE of  
 855 H, and H<sub>2</sub> of 148 K, and 627 K, respectively, are used from  
 856 Das et al. (2018) after scaling by 1.188, whereas in set 4, it is used

812 a species with the BE is considered by following  $E_b = RE_d$ ,  
 813 where,  $R$  may vary in between 0.35–0.8 (Garrod et al. 2007).  
 814 Here,  $R = 0.35$  and 0.50 are used to show their effects on  
 815 the chemical complexity. These BEs are either taken from

<sup>3</sup> <http://kida.astrophy.u-bordeaux.fr/>



857 650 K and 440 K, respectively for H, and H<sub>2</sub> (Wakelam et al.  
858 2017).  $R = 0.35$  is considered for both the set 3 and 4.

#### 859 4.1. Physical conditions

860 Here, a physical condition is used, which is suitable to ex-  
861 plain the properties of a hot core. Three models (Model A,  
862 Model B, and Model C) are implemented to describe the  
863 chemical complexity around this region. The physical condi-  
864 tion of our Model A is divided into three distinct phases. In  
865 the first phase ( $10^5$ - $10^6$  years), an isothermal (gas and grain  
866 temperature are kept the same) collapse of the cloud is con-  
867 sidered from a minimum hydrogen number density ( $n_{Hmin}$ )  
868  $3 \times 10^3 \text{ cm}^{-3}$  to a maximum hydrogen number density ( $n_{Hmax}$ )  
869  $10^7 \text{ cm}^{-3}$ . During this phase, the visual extinction param-  
870 eter ( $A_V$ ) can gradually increase due to increased density.  
871 The following relation between  $A_V$  and  $n_H$  is used to con-  
872 sider this situation (Lee et al. 1996; Gorai et al. 2020; Das &  
873 Chakrabarti 2011).

$$874 A_V = \max(A_{Vmin}, (\sqrt{n_H/n_{Hmin}} - 1) / (\sqrt{n_{Hmax}/n_{Hmin}} - 1) \times A_{Vmax}). \quad (7)$$

875 It is considered that  $A_V$  can vary from a minimum value  
876 ( $A_{Vmin} = 2$ ) to a maximum value ( $A_{Vmax} = 200$ ). In the second  
877 phase ( $5 \times 10^4$  years), the cloud remains constant at  $n_{Hmax}$ ,  
878  $A_{Vmax}$ . At the end of this phase, gas and dust temperature can  
879 reach up to 200 K. The third or last phase is a post warm-up  
880 phase (period of  $1.0 \times 10^5$  years), where  $n_H$ ,  $A_V$ , and temper-  
881 ature are kept fixed at their respective highest values.

882 In the case of Model B, the pre-stellar collapsing phase is  
883 considered instead of the initial isothermal collapsing phase.  
884 In this phase, the dust temperature is allowed to decrease as  
885 the collapse proceeds. Gas temperature is kept constant at 10  
886 K during this collapse. The other two phases are considered  
887 the same as Model A. Dust temperature of the pre-stellar col-  
888 lapsing phase is calculated by using the following empirical  
889 relation proposed by Hocuk et al. (2017) and used in Shi-  
monishi et al. (2020):

$$890 T_d^{Hoc} = [11 + 5.7 \tanh(0.61 - \log_{10}(A_V))] \chi_{uv}^{1/5.9}, \quad (8)$$

891 where  $\chi_{uv}$  is the Draine UV field strength (Draine 1978), cor-  
892 responding to  $1.7G_0$  using the Habing field (Habing 1968).  
893 Here,  $G_0$  is the Far Ultraviolet radiation field in the Habing  
894 unit ( $\sim 1.6 \times 10^{-3} \text{ erg cm}^{-2} \text{ s}^{-1}$ ) integrated over the energy  
895 range 6 – 13.6eV. Here,  $\chi_{uv} = 1$  is used.

896 Model C is the same as Model A. The only difference be-  
897 tween Model A and Model C is the isothermal collapsing  
898 time scale of the first phase. In Model C, a shorter time scale  
899 ( $10^5$  years) for the isothermal collapse is considered. It is  
900 more relevant for high mass star-forming regions. Thus, in  
901 the case of Model A, we have a density slope of  $\sim 10 \text{ cm}^{-3}$   
902 per year, whereas it is  $\sim 100 \text{ cm}^{-3}$  per year in the collapsing  
903 phase. The warm-up and post-warm-up timescales are kept  
the same as in Model A.

904 The physical condition described here are summarized in  
905 Figure 3. The time evolution of density, temperature, and  
906 visual extinction in the three distinct phases are shown for  
907 Model A, Model B, and Model C. The left axis of Figure 3  
908 represents the variation of temperature and visual extinction  
909 parameter in the linear scale, whereas the right axis repre-  
910 sents the density curve in the logarithmic scale. For the better  
911 visibility, in the top panel, temperature is plotted by scaling  
912 by a factor of 2. Model A and Model B start with an isother-  
913 mal collapsing phase. In this case, the dust temperature and  
914 gas temperature are kept the same. Here, a region having an  
915 initial temperature between 8 – 20 K is explored to check the  
916 sensitivity of our Model A on the initial choice of the ini-  
917 tial temperature. The temperature range for the initial phase  
918 of Model A and Model C is highlighted with the red shaded  
919 region. The visual extinction for the initial phase (isother-  
920 mal collapsing phase) of Model A and C is kept constant at  
921 2. In the case of Model B, the gas temperature of the 1<sup>st</sup>  
922 phase is kept fixed at 10 K, and dust temperature is estimated  
923 based on equation 8. The initial visual extinction of Model B  
924 is varied in between 0.1 – 10 (corresponds to an initial dust  
925 temperature of 16 – 5 K from equation 8) to check its effect  
926 on chemical evolution. The initial choice of visual extinction  
927 parameter and its estimated dust temperature of Model B are  
928 highlighted in green and yellow, respectively, in Figure 3. In  
929 the warm-up phase of Model A, Model B, and Model C,  $A_V$   
930 and  $n_H$  are kept constant at their highest value, and the tem-  
931 perature is allowed to increase up to 200 K. It is the typical  
932 temperature of a hot core (Garrod et al. 2008). In the post-  
933 warm-up phase, both the models have identical conditions.

## 934 4.2. Modeling results

### 935 4.2.1. Abundances

936 In Model A, various cases starting with the initial temper-  
937 ature between 8 – 20 K are considered. Figure 4 shows the  
938 variation of peak abundances with respect to H<sub>2</sub> obtained dur-  
939 ing the simulation time scale. Six pairs of aldehyde-alcohol,  
940 one pair of ketone-alcohol, and one pair of ketene-alcohol  
941 shown. Observed abundances in G10, G31, Sgr B2(N), and  
942 Orion KL are shown in solid blue, red, cyan, and orange  
943 curves, respectively. In Figure 4, the violet solid line rep-  
944 represents the case with set 1 BEs reported in Table 7. The solid  
945 black line represents the case with set 2. A lower value of  
946  $R$  provides more mobility to the surface species keeping the  
947 same resident time on grains. It yields a dramatic change in  
948 the production of surface species. The changes in the chem-  
949 ical composition of interstellar ice would reflect a significant  
950 difference between the gas phase abundances of the species  
951 shown in Figure 4. The case with set 3 is represented with the  
952 solid green line in Figure 4. The set 4 case is with the solid  
953 brown curve in Figure 4. It is evident from Figure 4 that the  
954 resulting peak abundance is highly sensitive on the choice of

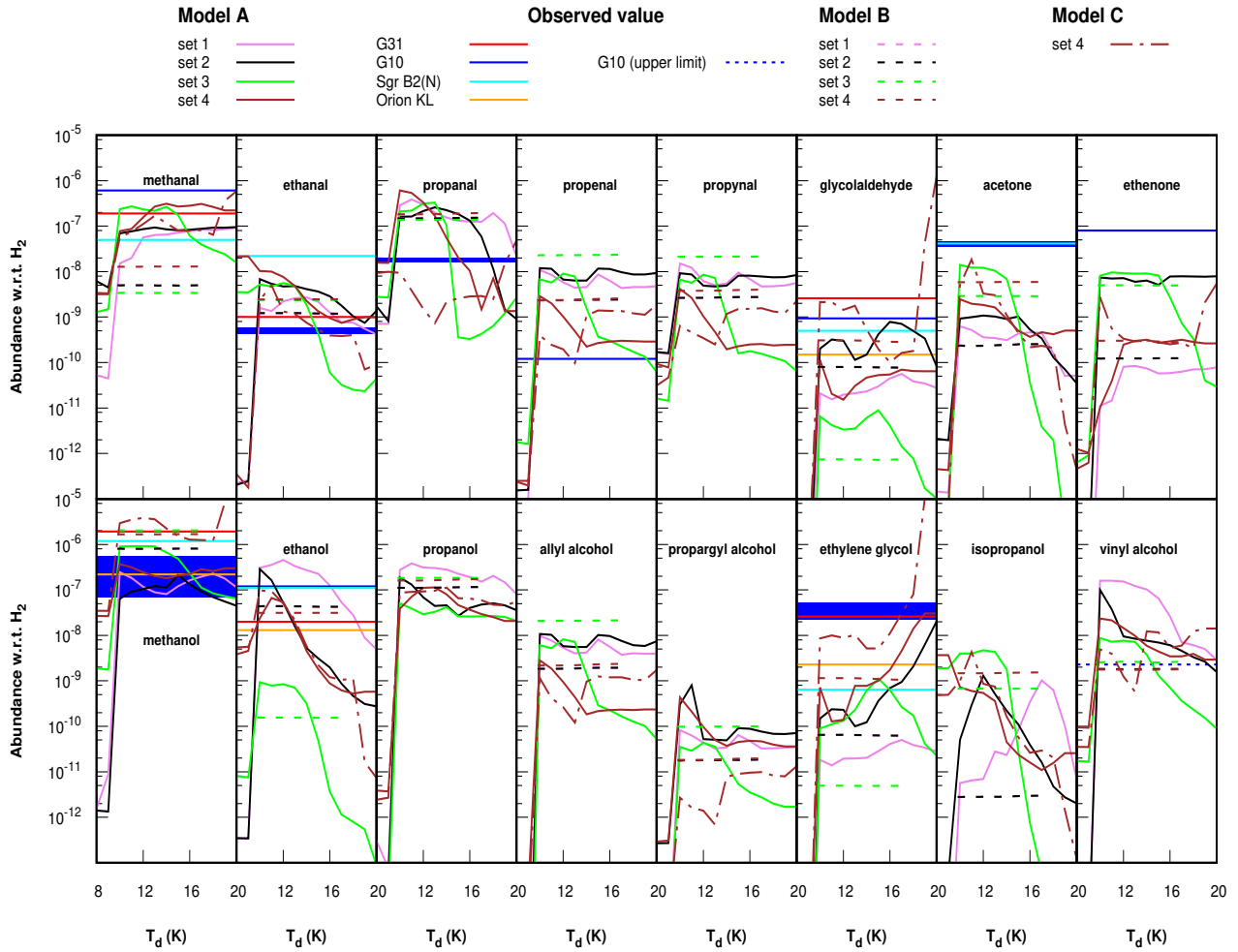


**Figure 4.** The initial dust temperature versus the peak gas-phase abundance obtained from Model A, Model B, and Model C is shown in various cases. Eight pairs of species are shown. Observed/upper-limit of the abundances of these species are marked with red (G31), blue (G10), Sgr B2(N) (cyan), and Orion KL (orange) if available. Since, in G10, some species are identified here, observed errors are shown with the thick blue curve. The solid curve represents the cases with Model A and dashed curves represent the same cases for Model B. Results obtained with Model C and set 4 are shown with the dashed-dot lines. The lower eight panels show the peak abundance variation of alcohols whereas the top panels show their related aldehyde, ketone, and ketene respectively. Thus, we conclude that there is both observational and theoretical evidence for production of alcohols via hydrogenation of precursor aldehydes, ketones and ketenes.

955 initial temperature. More specifically, on the dust tempera-  
 956 ture. Some cases of Model A are tested with a different gas  
 957 temperature than dust and did not find significant differences  
 958 in the peak abundance.

959 It is noticed that set 1 and set 2 BEs are helpful to explain  
 960 the abundances of these aldehydes and alcohols except gly-  
 961 colaldehyde and ethylene glycol. The set 3 BEs deviate very  
 962 much from the observed value. It is mainly because of the  
 963 adopted BE values of H (148 K) and H<sub>2</sub> (627 K). However,  
 964 with the set 4 BEs, the observed abundance of ethylene gly-  
 965 col could be explained. It is because set 4 considered the  
 966 BE of H and H<sub>2</sub> same as these are in set 1 and set 2 (650  
 967 K and 440 K, respectively for H and H<sub>2</sub>). The ice phase

968 origin of these species is evident from the results obtained  
 969 from Model A. The results obtained from Model A seem to  
 970 be highly sensitive to the initial dust temperature, which sug-  
 971 gests that either these species were formed during the initial  
 972 cold phase or the seeds of these species were produced dur-  
 973 ing the initial stage. The final gas-phase abundance of these  
 974 species is highly affected by the surface species present at  
 975 the beginning of the warm-up phase. The surface species at  
 976 the warm-up phase are re-processed with the elevated tem-  
 977 perature, where radicals take an active part in building the  
 978 chemical complexity. Once the warm-up phase starts, the  
 979 desorption of the surface species enhances and might reach  
 980 their respective sublimation temperatures and populate the

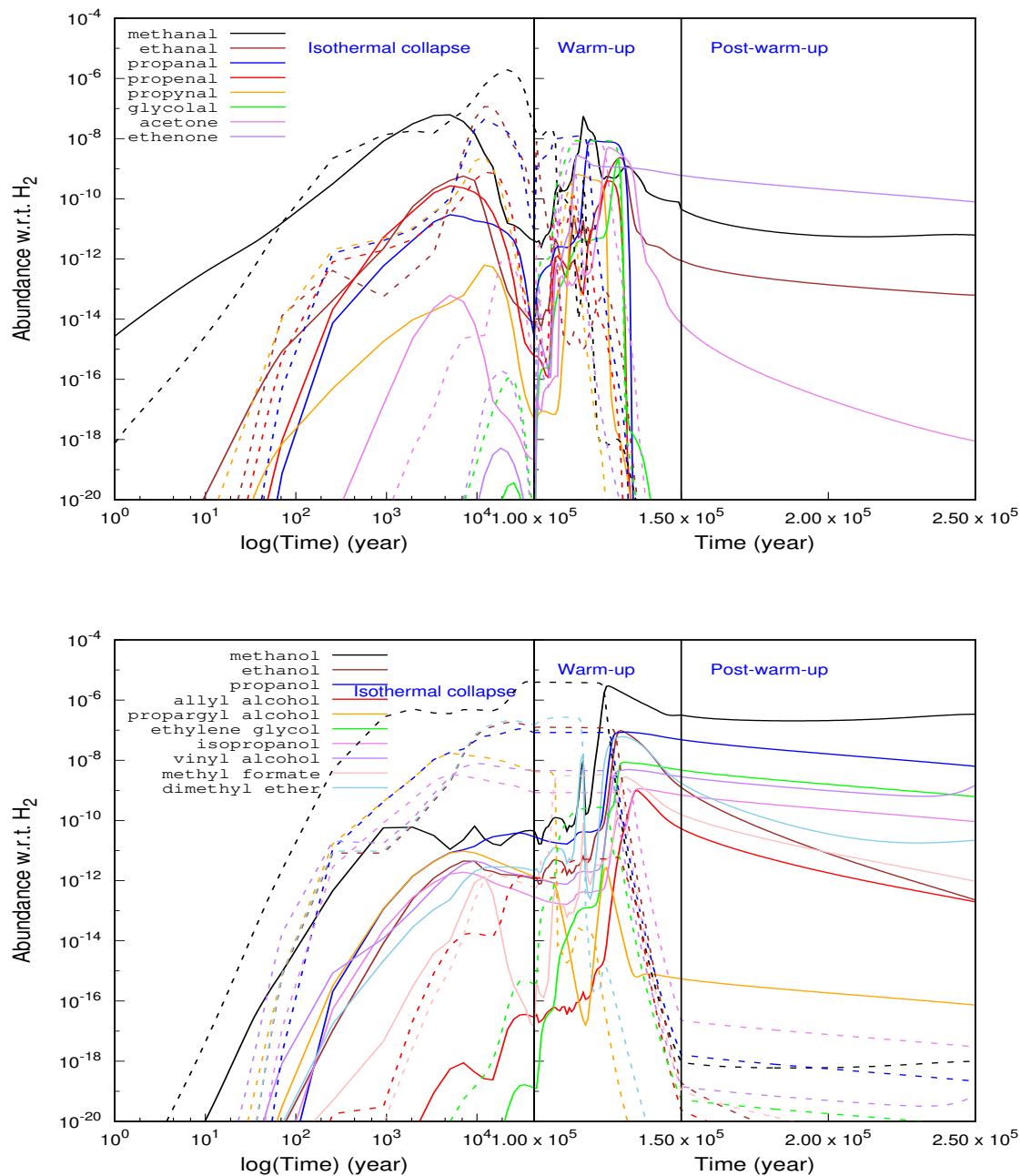


**Figure 5.** The chemical evolution of aldehyde, ketone, ketene and their corresponding alcohols are shown with the set 4 of CMMC Model C while initial dust temperature kept at 10 K. The X-axis of the figure shows the logarithmic scale for the isothermal collapsing phase, whereas, beyond that, it is shown on the regular scale. Gas phase abundance are represented with the solid curve whereas for the ice phase it is with the dashed curve. Additionally, the time evolution of propynal, methyl formate, and dimethyl ether are shown.

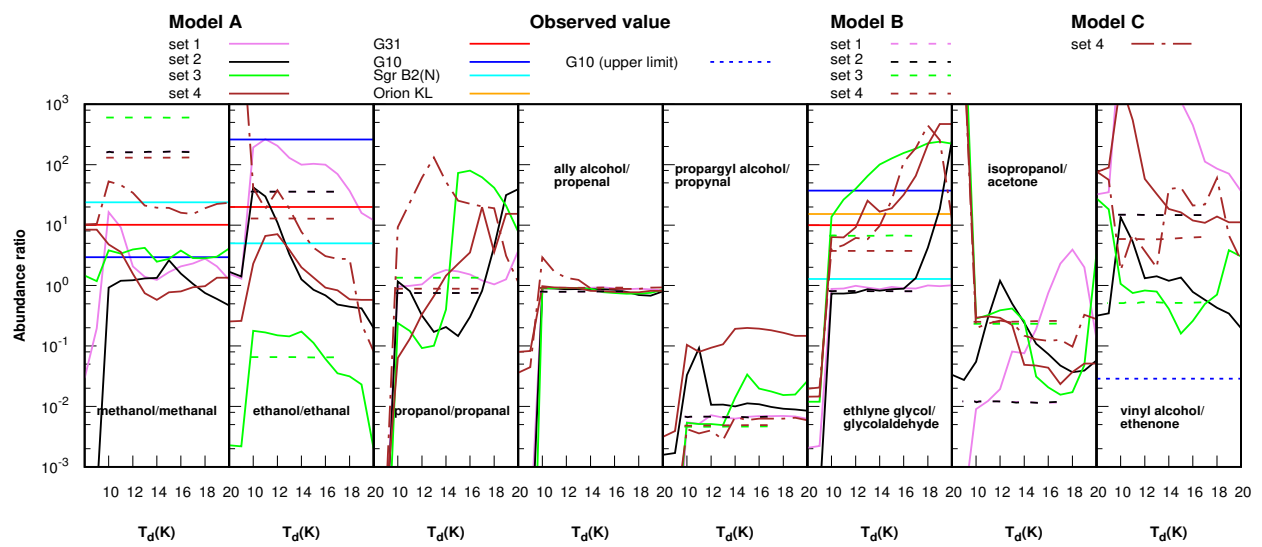


**Figure 6.** The obtained ratio in between six pairs of alcohol and aldehyde along with the ratio of alcohol-ketone and alcohol-ketene is shown. The observed ratio is marked in red (G31), blue (G10), cyan (Sgr B2(N)), and orange (Orion KL). Model A results are highlighted with solid curves whereas the same with Model B is represented with dashed curves and with Model C is represented with dot-dashed curves.

gas phase. With set 4 BE and Model A, it is possible to explain the observed abundances except glycolaldehyde.

The results obtained with Model B are also shown in Figure 4. All the four cases mentioned in the context of Model A are also considered with Model B. To visualize the differences between Model A and Model B, Model B cases are highlighted with the dashed curves, but with the same color codes. It is interesting to note that for Model B, significant changes of abundance for the adopted BE parameters are noticed. Like Model A, the results of Model B are not so much sensitive to the initial choice of dust temperature. The reason behind this deviation is the adopted dust temperature at the 1<sup>st</sup> phase of Model A and Model B (see Figure 3). In Model A, the dust remains at a constant temperature for  $\sim 10^6$  years, whereas in Model B, in between a few times  $10^3$  years, it drops down to temperature  $< 10$  K. This affects the mobility of the surface species. Since it stays at  $< 10$  K during its first phase of evolution, Model B does not show dramatic changes between the variation of the initial dust temperature.

The orange curve of Figure 4 represents the variation of the peak abundances of these species with set 4 and Model C. It is interesting to note that with the shorter collapsing time scale (relevant for the hot core) of Model C, peak abundances of complex organic molecules are significantly enhanced. Most of the observed abundances could be explained with set 4 of Model C. The increase in the abundances of the complex organic molecule with the shorter collapsing time is not so straightforward. Many parameters are involved in it. But the shorter collapsing time leads to a much steeper slope for the density, which means that the depletion will be much faster and the complex molecules, once produced, will have a comparatively shorter time to be destroyed further. In Figure 5, the time evolution of the gas phase and ice phase abundances of aldehydes, alcohols, ketone, and ketene with respect to  $H_2$  are shown. Only the results obtained with Model C by considering an initial gas and ice temperature of 10 K is shown. There is some uncertainty in the observations. Additionally, the chemical model includes lots of estimated parameters (BEs, reaction pathways, reaction rates, interaction with dust, etc.) that can induce severe skepticism. Due to these reasons, it is not easy to match all the observed abundances simultaneously. In Figure 4, the peak abundance is taken beyond the isothermal collapsing phase. Figure 5, depicts that beyond the isothermal phase these peak gas-phase abundance appeared during the warm-up phase, when the temperature varies in between  $\sim 100 - 120$  K. So our time uncertainty is relatively small ( $\sim 10^4$  years).

A comparison between our obtained gas-phase peak abundance with the observational results is shown in Table 6. Only the results obtained with set 4 of Model C are used to show this comparison. Minimum and maximum peak abundances obtained within the initial temperature range consid-

ered for Model C and set 4 are noted in Table 6. The errors in obtained abundances are only shown for those species which are identified herein G10. The errors are calculated by taking the uncertainty in estimating the  $H_2$  column density and the column density obtained from rotation diagram analysis. Gorai et al. (2020) obtained an average column density of  $\sim 1.35 \times 10^{25} \text{ cm}^{-2}$ . The error in estimating the column density was  $\pm 1.0 \times 10^{22} \text{ cm}^{-2}$ , which mainly arose from the uncertainty of the measured flux. The error in estimating the column density of the species is taken from Table 2. For estimating the abundance errors for glycolaldehyde, only the uncertainty in predicting the  $H_2$  column density is considered.

It is noticed that our results can successfully explain the observed abundances.

#### 4.2.2. Molecular ratios

In Figure 6, the temperature variation of the ratio obtained between the peak abundance of six pairs of alcohol-aldehyde, one pair of alcohol-ketone, and one pair of alcohol-ketene for Model A (solid curve), Model B (dashed curve), and Model C (dot-dashed curves) are shown. The observed ratios for G31, G10, Sgr B2(N), and Orion KL are shown with red, blue, cyan, and orange solid lines, respectively. The simulated ratio between the peak abundance of alcohol and aldehyde/ketone/ketene obtained with set 4 and Model C, along with the observed abundances of these species is noted in Table 6. Table 6 depicts the observed abundances in G31, G10, Sgr B2, and Orion KL, along with our modeled abundance. Mainly the interferometric observations (wherever available) are noted to facilitate a comparative study between the chemical complexity of these hot cores. However, it is worth pointing out that all these observations are carried out with different facilities with very diverse angular and spatial resolutions. The facility used for each observations along with the  $H_2$  column density used to derive the abundances are noted at the footnote of Table 6. Here, the band 4 archival data of G10 is only analyzed, which reports only one alcohol-aldehyde pair (ethylene glycol-glycolaldehyde pair). These two species are recognized for the first time in this source. Earlier, Rolffs et al. (2011) obtained the methanol-methanal pair. Any transitions of methanal are not identified within our spectral bands. So, a direct comparison between our obtained ratios and others could not be performed. For example, Table 6 denotes a higher methanol abundance obtained by Rolffs et al. (2011) than ours. This is because the beam size of our band 4 observation of ALMA varies between  $1.39'' - 2.44''$  ( $\sim 12000 - 21000$  AU, considering 8.6 kpc distance). In contrast, the beam size of the submillimeter Array (SMA) observation at 345 GHz of Rolffs et al. (2011) is  $0.3''$  ( $\sim 2600$  AU, considering 8.6 kpc distance). The integrated emission map of the methanol transitions shown in

Figure C3 suggests that the methanol is more compact. So as expected, with the higher spatial resolution, Rolffs et al. (2011) can trace the more inner region of the G10, and thus they obtained a higher abundance than us. Furthermore, for deriving the abundances from Rolffs et al. (2011), a hydrogen column density of  $5 \times 10^{24} \text{ cm}^{-2}$  is used. In contrast, our abundance is derived by considering  $1.35 \times 10^{25} \text{ cm}^{-2}$  (Gorai et al. 2020), which might also create significant variation. Since our chemical model does not consider the spatial variation of the abundances, explaining the observed ratio with the suitable beam size is also out of scope for this work.

The observed ratio is calculated from the observed pair from the same source (if available). It depicts that the methanol to methanal abundance ratio in these sources can vary between 2.95–23.8, whereas our calculated methanol to methanal ratio varies between 10–53. The observed ratio between ethanol to ethanal varies between 5–261, whereas our model results show it ranges between 0.08–25600. The observed ethylene glycol to glycolaldehyde ratio varies between 1.3–37, whereas our model derives 0.019–445. The observed ratio between the vinyl alcohol to ethenone is 0.021, whereas our chemical model estimates 1.78–77. In brief, the observed ratio of three alcohol-aldehyde pairs (methanal-methanol, ethanal-ethanol, glycolaldehyde-ethylene glycol) is  $> 1$  in G10, G31, Sgr B2(N), and Orion KL. Thus, in the high-mass star-forming regions, the abundances of these alcohols are generally higher than their respective aldehydes. Our estimated molecular ratios for these alcohol-aldehyde pairs are similar to the observed values in the temperature range 12–18 K (see Figure 6). However, in the case of the vinyl alcohol to ethenone, the observed abundance ratio could not be explained. It could be because of the consideration of the upper limit of vinyl alcohol observation from the single-dish observation of Dickens et al. (2001) for deriving the molecular ratio. A little ambiguity between our obtained ratio of the dimethyl ether (DE) and methyl formate (MF) is obtained. DE/MF  $< 1$  is received from our observational analysis, whereas Rolffs et al. (2011) noted it  $> 1$  for the same source. Also, in other high mass sources, the ratio is  $> 1$  (4.5 for Sgr B2, 2 for G31, and 2.5 for the Orion KL). Our modeling results find that the ratio of DE with the MF can vary between 0.12–152.

## 5. CONCLUSIONS

Here, our CMMC model coupled with the observational study is used to explain the abundance of some interstellar aldehydes, ketone, ketene, along with their corresponding alcohols. It is noticed that there is both observational and theoretical evidence for production of alcohols via hydrogenation of precursor aldehydes, ketones and ketenes. The following are the main highlights of this paper.

- Various aldehydes, alcohols, and a ketone are identified in G10. Among them, ethylene glycol and propanal are detected for the first time in G10, and glycolaldehyde is tentatively detected.
- The column densities and fractional abundances of the observed molecules are estimated assuming LTE conditions. The kinetic temperatures of the gas are also evaluated, which varies from 72 K to 234 K.
- The spatial distributions of the observed species are investigated, and their zeroth-order moment maps and emitting regions are provided. However, molecular emissions are not well spatially resolved or, at best, marginally resolved. Thus, we need high angular resolution data to understand their detail distributions in G10.
- Successive hydrogenation reaction can lead to the formation of alcohol starting from the aldehyde/ketone/ketene. Extensive quantum chemical calculations are carried out to yield the TS of some of these reactions. The first step of the hydrogen addition reactions has an activation barrier, whereas the second step could be considered barrier-less radical-radical reactions. Our higher-level (CCSD(T)/aug-cc-pVTZ) ice-phase calculations depict the first step of hydrogenation reaction at the carbon atom position for all the pairs (except acetone-isopropanol) is comparatively favorable than the oxygen atom position. In the acetone-isopropanol couple, an actual TS could not be obtained for the hydrogenation to the carbon atom position. However, the lower-level calculation (DFT-B3LYP/6-31+G(d,p)) in the ice-phase shows the same trend.
- BEs of these species are computed with various substrates such as  $\text{H}_2\text{O}$ ,  $\text{CH}_3\text{OH}$ , and  $\text{CO}$ . For most cases, the BE of alcohols is found to be greater than that of the corresponding aldehyde/ketone/ketene. On average, the computed BEs with  $\text{CH}_3\text{OH}$  monomer is found  $\sim 1.16$  times higher, and with  $\text{CO}$  monomer, it is  $\sim 2.85$  times lower than that of the water monomer. These new sets of BEs would help understand the chemical complexity, where  $\text{CO}$  and  $\text{CH}_3\text{OH}$  would also efficiently cover the icy mantle. BEs of the species reported in this study for the alcohol, aldehyde, ketone, and ketenes is a little bit on the higher side ( $\sim 3000$  K) with the  $\text{H}_2\text{O}$  c-tetramer configuration. Comparatively, a higher surface temperature is needed to transfer these surface species in the gas phase. Such a high temperature is usually achieved deep inside the cloud in the hot core phase. If the grain surface pathways are the only deriving route, then species with lower BE

1184 are expected to have more extended emission than the  
1185 species with relatively higher BE. Since our observed  
1186 beam size was large, it is not possible to spatially re-  
1187 solve the inner region and comment on the dependency  
1188 between the BE and size of the emitting region.

- 1189 • Our CMMC model with the shorter collapsing time  
1190 scale ( $\sim 10^5$  years) was able to reproduce the observed  
1191 abundance and observed ratio between various species.

#### ACKNOWLEDGMENTS

This paper makes use of the following ALMA data: ADS/JAO.ALMA#2016.1.00929.S. ALMA is a partnership of ESO (representing its member states), NSF (USA) and NINS (Japan), together with NRC (Canada), MOST and ASIAA (Taiwan), and KASI (Republic of Korea), in cooperation with the Republic of Chile. The Joint ALMA Observatory is operated by ESO, AUI/NRAO and NAOJ. S.K.M. acknowledges CSIR fellowship (Ref no. 18/06/2017(i) EU-V). P.G. acknowledges support from a Chalmers Cosmic Origins postdoctoral fellowship. M.S. gratefully acknowledges DST, the Government of India for providing financial assistance through the DST-INSPIRE Fellowship [IF160109] scheme. A.D. acknowledges ISRO respond project (Grant No. ISRO/RES/2/402/16-17) for partial financial support. J.C.T. acknowledges support from the Chalmers Foundation and VR grant. T.S. and A.D. acknowledge Indo-Japan Collaborative Science Programme. This research was possible in part due to a Grant-In-Aid from the Higher Education Department of the Government of West Bengal.

1192 *Software:* Gaussian 09 (Frisch et al. 2013), CASA 4.7.2  
1193 (McMullin et al. 2007), CASSIS (Vastel et al. 2015).

## APPENDIX

## A. EMITTING DIAMETER

The emitting diameter of each transition of the observed molecules is shown in Table A1. Here, the average emit-

ting diameter refers to the average source size. 2D Gaussian fittings of a region (area enclosing 50% line peak) of the moment map image are performed. After averaging the semi-minor and semi-major axis, the emission region's diameters are obtained.

**Table A1.** The emitting diameter of each transition of observed species toward G10.47+0.03.

Species	$J'_{K'_a K'_c} - J''_{K''_a K''_c}$	Frequency (GHz)	$E_u$ (K)	Emitting diameter (average) $\theta''_s$
Methanol (CH <sub>3</sub> OH)	11 <sub>0,11</sub> – 11 <sub>1,11</sub> E, vt=0	154.425832*	166.1	1.81
	12 <sub>0,12</sub> – 15 <sub>1,12</sub> E, vt=0	153.281282*	193.8	1.79
	15 <sub>0,15</sub> – 15 <sub>1,15</sub> E, vt=0	148.111993	290.7	1.78
	7 <sub>-1,7</sub> – 6 <sub>0,6</sub> E, vt=1	147.943673	356.3	1.56
	17 <sub>-4,13</sub> – 18 <sub>-3,16</sub> E, vt=0	131.134094	450.9	1.45
	21 <sub>0,21</sub> – 21 <sub>1,21</sub> E, vt=0	129.720384	546.2	1.33
	88 <sub>-7,1</sub> – 7 <sub>-6,1</sub> E, vt=1	153.128697	664.5	1.23
Ethylene Glycol (g-HOCH <sub>2</sub> CHO)	8 <sub>4,5</sub> – 7 <sub>3,5</sub> , 1-0	153.567383	25.4	1.83
	13 <sub>3,11</sub> – 12 <sub>2,10</sub> , 0-0	159.768239	48.8	1.85
	13 <sub>9,4</sub> – 12 <sub>9,3</sub> , 0-1	130.998583	83.8	1.04
	27 <sub>3,25</sub> – 27 <sub>2,26</sub> , 0-0	148.082465	185.5	1.04
	28 <sub>7,21</sub> – 28 <sub>6,23</sub> , 1-0	131.229156	223.4	1.21
	33 <sub>10,23</sub> – 32 <sub>11,22</sub> , 1-1	130.115657	323.0	1.60
39 <sub>8,32</sub> – 39 <sub>7,33</sub> , 1-1	153.325448	414	1.27	
Acetaldehyde (CH <sub>3</sub> CHO)	8 <sub>3,6</sub> – 7 <sub>3,5</sub> , A	154.2746864	53.7	1.49
	8 <sub>3,5</sub> – 7 <sub>3,4</sub> , E	154.296489	53.7	1.53
	8 <sub>4,4</sub> – 7 <sub>4,3</sub> , A	154.201471	69.5	1.38
	8 <sub>5,4</sub> – 7 <sub>5,3</sub> , A	154.161467	89.8	1.33
	8 <sub>3,5</sub> – 7 <sub>3,4</sub> , A	154.173895	114.4	1.0
Propanal (CH <sub>3</sub> CH <sub>2</sub> CHO)	9 <sub>7,2</sub> – 9 <sub>6,3</sub> , A	148.005042	49.6	1.18
	10 <sub>7,3</sub> – 10 <sub>6,4</sub> , E	147.867178	54.6	1.27
	16 <sub>2,15</sub> – 15 <sub>1,14</sub> , E	159.932346	68.6	0.83
	25 <sub>3,22</sub> – 25 <sub>2,23</sub> , A	153.554511	172.7	1.87
	27 <sub>5,23</sub> – 27 <sub>4,24</sub> , E	154.066288	206.2	1.08
Glycolaldehyde (HOCH <sub>2</sub> CHO)	15 <sub>0,15</sub> – 14 <sub>1,14</sub>	153.597995	60.5	1.26
	20 <sub>7,13</sub> – 20 <sub>6,14</sub>	153.614231	147.0	0.89
Acetone (CH <sub>3</sub> COCH <sub>3</sub> )	12 <sub>2,11</sub> – 11 <sub>1,10</sub> , AA	130.924799	44.1	1.28
	11 <sub>5,7</sub> – 10 <sub>4,6</sub> , EE	147.684364	48.4	1.83
	13 <sub>2,11</sub> – 12 <sub>3,10</sub> , AE	149.395864	55.8	1.56
	14 <sub>3,12</sub> – 13 <sub>2,11</sub> , EE	159.2476343	63.4	1.29

Table A1 continued



**Table A1** (*continued*)

Species	$J'_{K'_a K'_c} - J''_{K''_a K''_c}$	Frequency	$E_u$	Emitting diameter (average)
		(GHz)	(K)	$\theta''_s$
	22 <sub>4,18</sub> – 22 <sub>3,19</sub> , EE	160.118153	157.1	1.38
	24 <sub>6,18</sub> – 24 <sub>5,19</sub> , EE	159.415955	198.9	1.50
	25 <sub>10,15</sub> – 25 <sub>9,16</sub> , AE	130.708968	241.0	1.0
	26 <sub>10,17</sub> – 26 <sub>9,18</sub> , EE	149.190766	251.0	1.35
Methyl formate (CH <sub>3</sub> OCHO)	11 <sub>2,10</sub> – 10 <sub>2,9</sub> , A	130.016790	40.7	1.87
	11 <sub>2,10</sub> – 10 <sub>2,9</sub> , E	130.010105	40.7	1.80
	12 <sub>4,9</sub> – 11 <sub>4,8</sub> , A	148.805941	56.8	1.95
	13 <sub>3,11</sub> – 12 <sub>3,10</sub> , A	158.704392	59.6	1.85
	13 <sub>7,6</sub> – 12 <sub>7,5</sub> , A	160.178942	86.2	1.82
	13 <sub>7,6</sub> – 12 <sub>7,5</sub> , A	160.193496	86.2	1.66
	13 <sub>10,4</sub> – 12 <sub>10,3</sub> , A	159.662793	120.0	1.67
	12 <sub>1,12</sub> – 11 <sub>1,11</sub> , A	131.377495	230.0	1.0
	12 <sub>4,8</sub> – 11 <sub>4,7</sub> , E	148.575217	244.1	1.69
Dimethyl ether (CH <sub>3</sub> OCH <sub>3</sub> )	6 <sub>1,6</sub> – 5 <sub>0,5</sub> , AA	131.406552	19.9	1.91
	9 <sub>0,3</sub> – 8 <sub>1,8</sub> , AE	153.055196	40.4	1.83
	11 <sub>1,10</sub> – 10 <sub>2,9</sub> , AE	154.456506	62.9	1.95
	24 <sub>4,20</sub> – 24 <sub>3,21</sub> , EE	153.385902	297.5	1.44

NOTE— \* optically thick

## B. OBSERVED SPECTRA TOWARD G10

1203

1204 The observed, fitted and LTE spectra of observed transi-  
 1206 tions are shown in Figure B1.

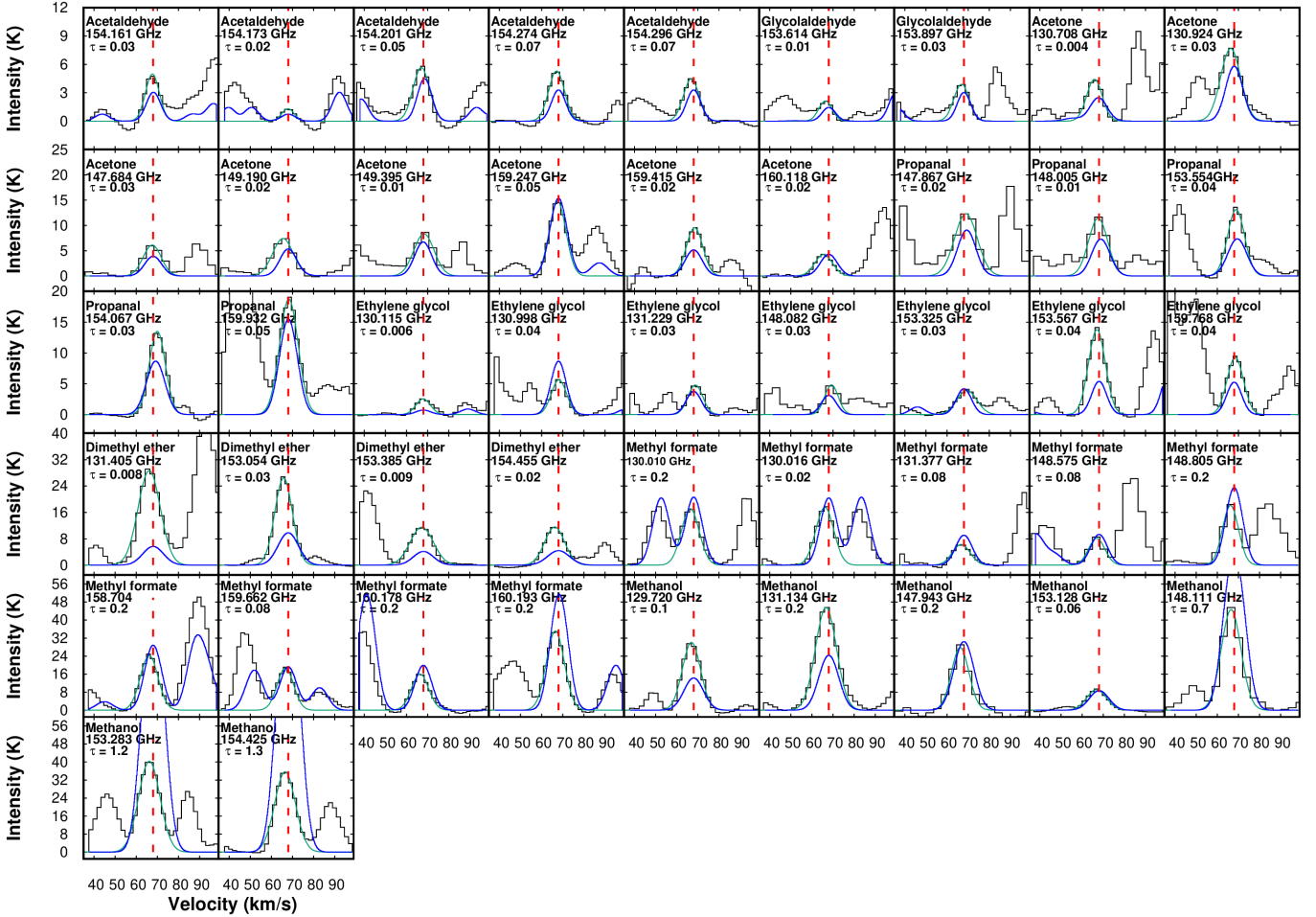


**Figure B1.** The observed spectra (solid black lines) along with the fitted Gaussian profile (solid green lines) and the LTE synthetic spectrum with our derived parameters (rotation temperature and column density) from rotational diagram analysis with the solid blue lines are shown. For the LTE calculation, a source size of 2'' and average FWHM obtained from the Gaussian fitting (noted in Table 1) of each species are used. The dashed red line shows the systematic velocity ( $V_{LSR}$ ) of the source at  $\sim 68$  km s<sup>-1</sup>. In addition, the name of the species and their respective transitions (in GHz) and optical depth of each transitions are given in each panel. Optical depth of all transitions are calculated based on the parameters assumed during LTE modeling. The last two transitions of methanol are optically thick, which are largely overproduced with the LTE consideration. The intensity of all the transitions of dimethyl ether is underproduced, possibly because our overestimated FWHM for dimethyl ether.

## C. LINE MAPS

1207

1208 The integrated intensity distribution of all observed  
1209 molecules is shown in Figures C1, C2, C3, and C4. The  
1210 integrated intensity is obtained in the velocity range where  
1211 the emission line is seen. It is typically obtained between  
1212 58 km/s to 78 km/s. This range slightly varies for some  
1213 species. Figures C1 and C2 show the intensity distribution  
1214 of the observed molecules having upper energy state < 100  
1215 K and Figures C3 and C4 show the intensity distribution for  
1216 the molecules with upper energy state > 100 K.

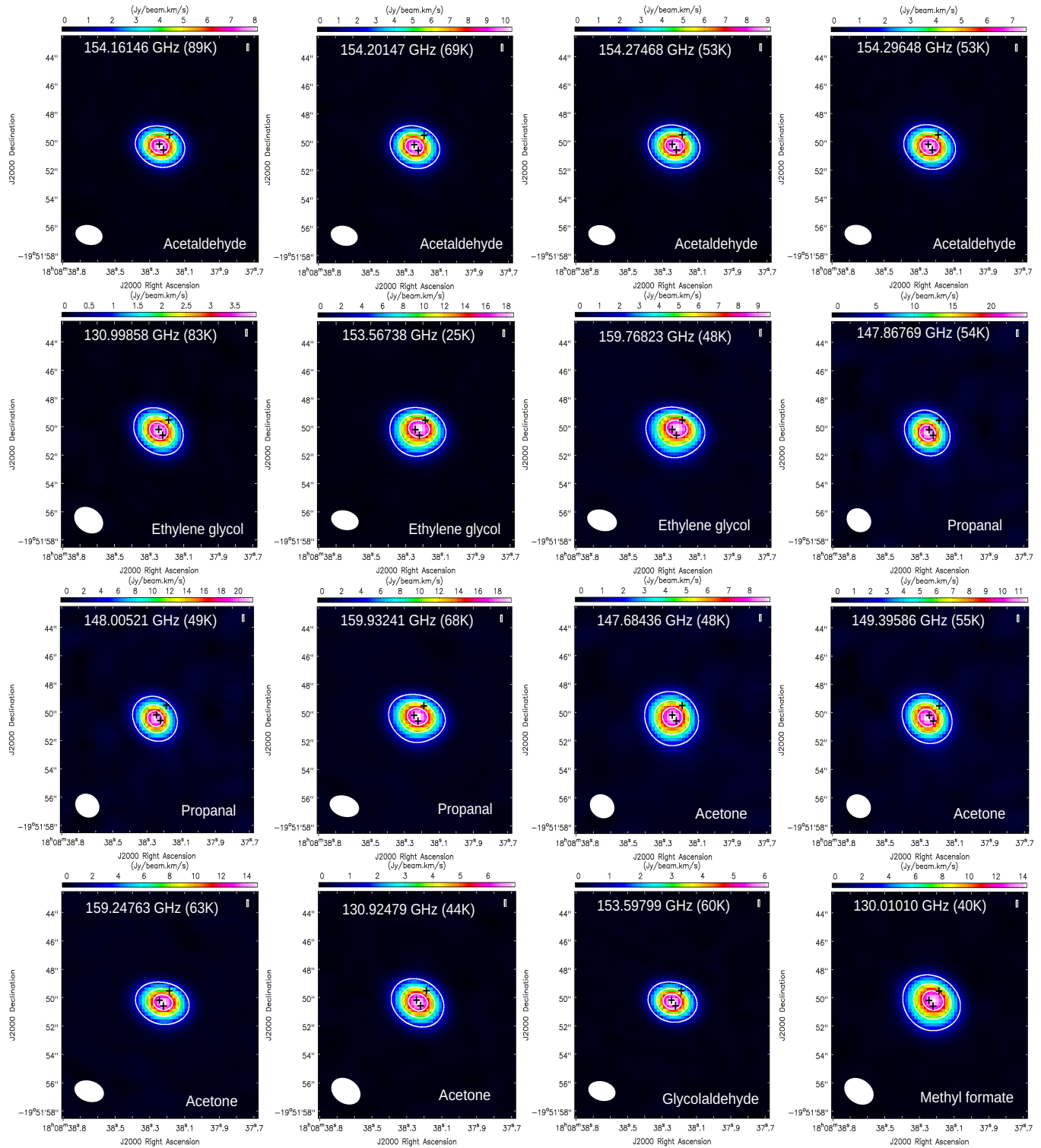


**Figure C1.** Integrated emission maps of observed transitions with upper energy state less than 100 K. Name of the molecules along with their respective transitions (in GHz) and upper energy state (in K) are given in each panel. The contours are shown at 20, 50, and 80% of maximum flux. The observed beam is shown in the lower-left corner of each figure. Three blue plus signs indicate the HII regions B1, B2, and A in the anticlockwise direction starting from the left black cross situated in the white and pink zones of continuum images (Cesaroni et al. 2010).

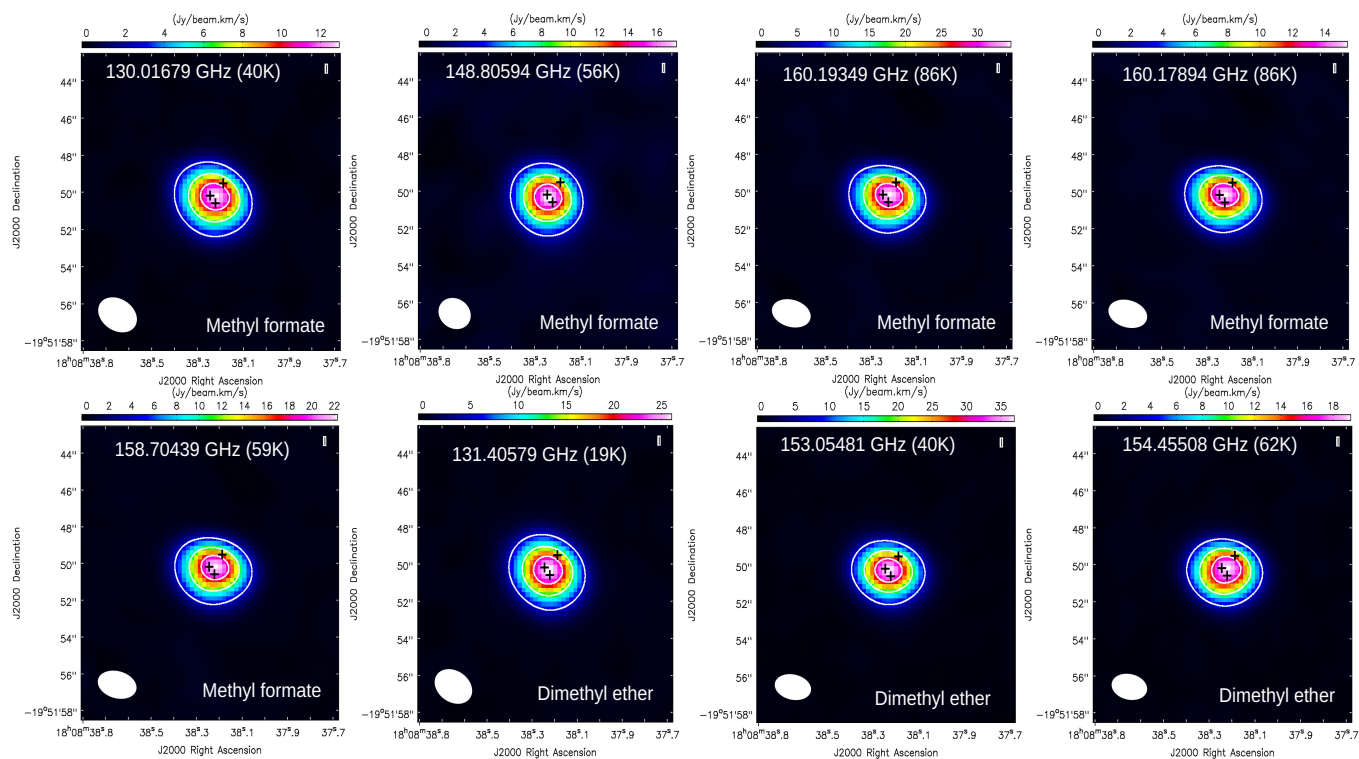
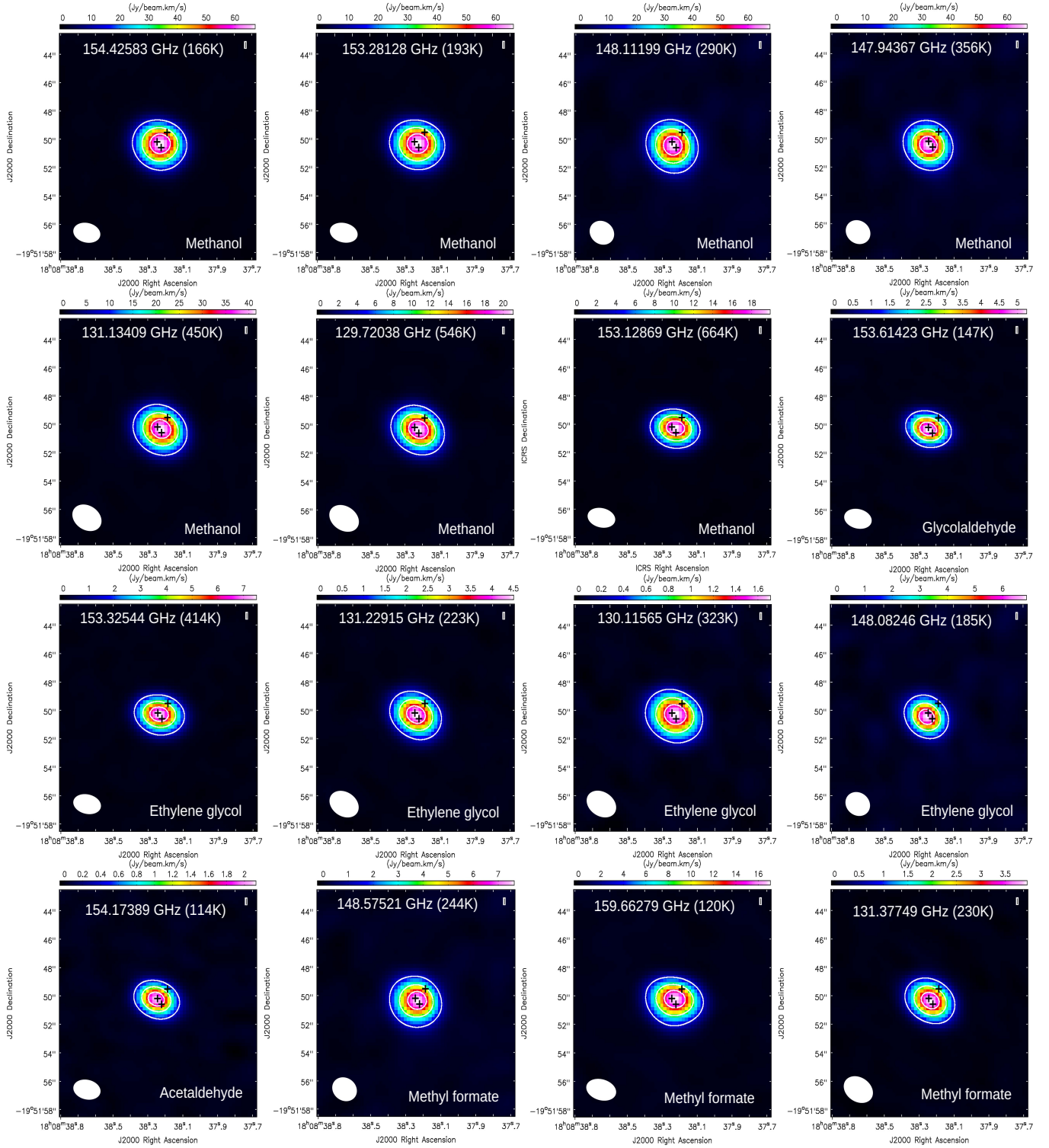


Figure C2. Same as Figure C1.



**Figure C3.** Integrated emission maps of observed transitions with upper energy state greater than 100 K are shown. The contours are shown at 20, 50, and 80% of maximum flux. The observed beam is shown in the lower-left corner of each figure. Three blue plus signs indicate the HII regions B1, B2, and A in the anti-clockwise direction starting from the left black cross situated in the white and pink zones of continuum images (Cesaroni et al. 2010).

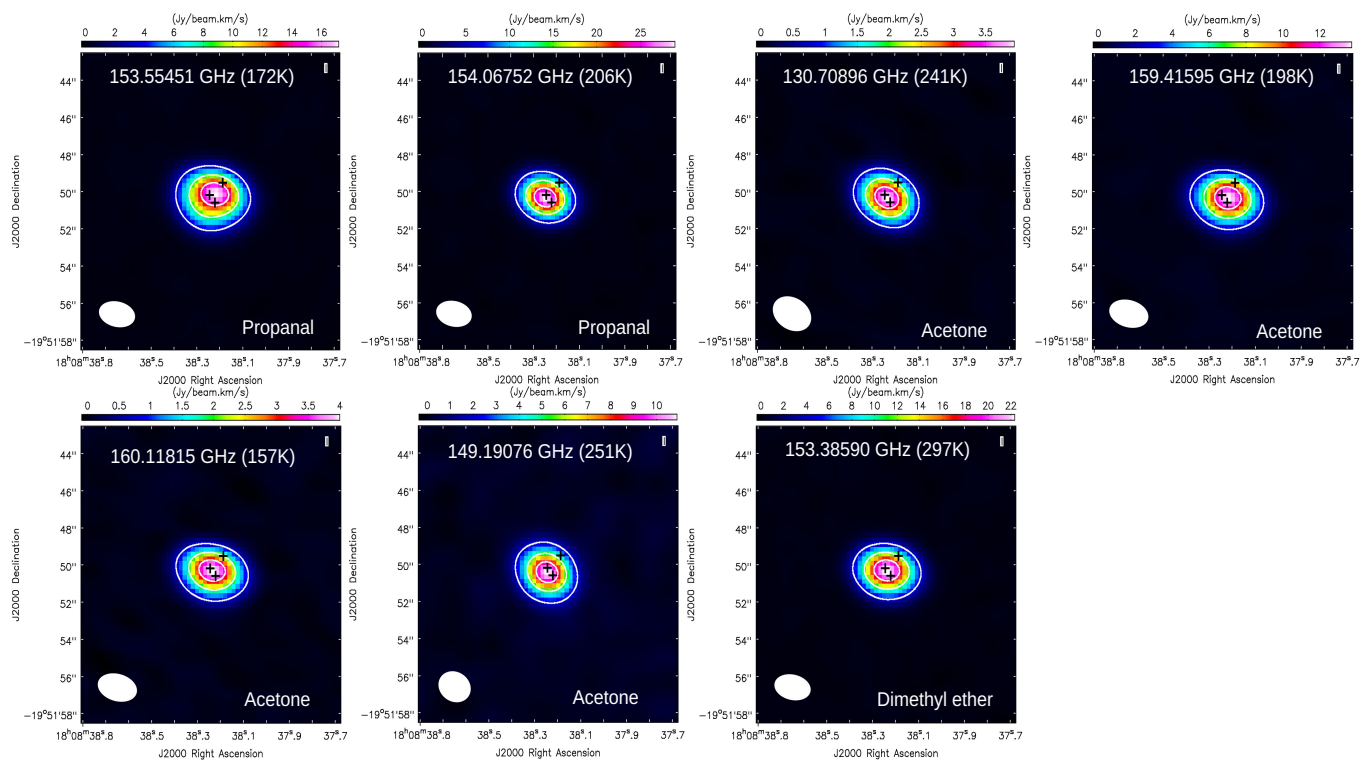


Figure C4. Same as Figure C3.

## REFERENCES

- 1217 Allamandola, L. J., Sandford, S. A., Tielens, A. G. G. M., &  
1218 Herbst, T. M. 1992, *ApJ*, 399, 134
- 1219 Altwegg, K., Balsiger, H., Berthelier, J. J., et al. 2017, *MNRAS*,  
1220 469, S130
- 1221 Álvarez-Barcia, S., Russ, P., Kästner, J., & Lamberts, T. 2018,  
1222 *MNRAS*, 479, 2007
- 1223 Aragonés, J. L., MacDowell, L. G., & Vega, C. 2011, *Journal of*  
1224 *Physical Chemistry A*, 115, 5745
- 1225 Becke, A. D. 1993, *The Journal of Chemical Physics*, 98, 5648
- 1226 Belloche, A., Garrod, R. T., Müller, H. S. P., & Menten, K. M.  
1227 2014, *Science*, 345, 1584
- 1228 Belloche, A., Müller, H. S. P., Menten, K. M., Schilke, P., &  
1229 Comito, C. 2013, *A&A*, 559, A47
- 1230 Beltrán, M. T., Codella, C., Viti, S., Neri, R., & Cesaroni, R. 2009,  
1231 *ApJL*, 690, L93
- 1232 Bhat, B., Gorai, P., Mondal, S. K., Chakrabarti, S. K., & Das, A.  
1233 2021, Radiative transfer modeling of the observed line profiles  
1234 in G31.41+0.31, , , arXiv:2107.04979
- 1235 Bisschop, S. E., Fuchs, G. W., van Dishoeck, E. F., & Linnartz, H.  
1236 2007, *A&A*, 474, 1061
- 1237 Bisschop, S. E., Jørgensen, J. K., Bourke, T. L., Bottinelli, S., &  
1238 van Dishoeck, E. F. 2008, *A&A*, 488, 959
- 1239 Biver, N., Bockelée-Morvan, D., Debout, V., et al. 2014, *A&A*,  
1240 566, L5
- 1241 Brouillet, N., Despois, D., Lu, X. H., et al. 2015, *A&A*, 576, A129
- 1242 Butscher, T., Duvernay, F., Rimola, A., Segado-Centellas, M., &  
1243 Chiavassa, T. 2017, *Physical Chemistry Chemical Physics*  
1244 (Incorporating Faraday Transactions), 19, 2857
- 1245 Cancès, E., Mennucci, B., & Tomasi, J. 1997, *Journal of Chemical*  
1246 *Physics*, 107, 3032
- 1247 Carr, R. W., J., Gay, I. D., Glass, G. P., & Niki, H. 1968, *JChPh*,  
1248 49, 846
- 1249 Cesaroni, R., Hofner, P., Araya, E., & Kurtz, S. 2010, *A&A*, 509,  
1250 A50
- 1251 Cesaroni, R., Hofner, P., Walmsley, C. M., & Churchwell, E. 1998,  
1252 *A&A*, 331, 709
- 1253 Chaabouni, H., Bergeron, H., Baouche, S., et al. 2012, *A&A*, 538,  
1254 A128
- 1255 Chakrabarti, S. K., Das, A., Acharyya, K., & Chakrabarti, S.  
1256 2006a, *A&A*, 457, 167
- 1257 —. 2006b, *Bulletin of the Astronomical Society of India*, 34, 299
- 1258 Chang, Q., Zheng, X.-L., Zhang, X., et al. 2021, *Research in*  
1259 *Astronomy and Astrophysics*, 21, 039
- 1260 Charnley, S. 2001, *The bridge between the big bang and biology*,  
1261 ed, Vol. 139 (F. Giovannelli, Rome: Consiglio Nazionale delle  
1262 Ricerche)
- 1263 Chuang, K. J., Fedoseev, G., Ioppolo, S., van Dishoeck, E. F., &  
1264 Linnartz, H. 2016, *MNRAS*, 455, 1702
- 1265 Collins, P., Ferrier, R., & Berlin, W. 1995, *Analytical*  
1266 *Biochemistry*, 230, 359
- 1267 Combes, F., Gerin, M., Wootten, A., et al. 1987, *A&A*, 180, L13
- 1268 Cooper, G., Kimmich, N., Belisle, W., et al. 2001, *Nature*, 414, 879
- 1269 Córdova, A., Ibrahim, I., Casas, J., et al. 2005, *Chemistry*  
1270 (Weinheim an der Bergstrasse, Germany), 11, 4772—4784
- 1271 Coutens, A., Viti, S., Rawlings, J. M. C., et al. 2018, *MNRAS*, 475,  
1272 2016
- 1273 Crovisier, J., Bockelée-Morvan, D., Biver, N., et al. 2004, *A&A*,  
1274 418, L35
- 1275 Das, A., Acharyya, K., Chakrabarti, S., & Chakrabarti, S. K.  
1276 2008a, *A&A*, 486, 209
- 1277 Das, A., Acharyya, K., & Chakrabarti, S. K. 2010, *MNRAS*, 409,  
1278 789
- 1279 Das, A., & Chakrabarti, S. K. 2011, *MNRAS*, 418, 545
- 1280 Das, A., Chakrabarti, S. K., Acharyya, K., & Chakrabarti, S.  
1281 2008b, *NewA*, 13, 457
- 1282 Das, A., Gorai, P., & Chakrabarti, S. K. 2019, *Astronomy &*  
1283 *Astrophysics*, 628, A73
- 1284 Das, A., Majumdar, L., Chakrabarti, S. K., & Sahu, D. 2015b,  
1285 *NewA*, 35, 53
- 1286 Das, A., Majumdar, L., Sahu, D., et al. 2015a, *ApJ*, 808, 21
- 1287 Das, A., Sahu, D., Majumdar, L., & Chakrabarti, S. K. 2016,  
1288 *MNRAS*, 455, 540
- 1289 Das, A., Sil, M., Ghosh, R., et al. 2021, *Frontiers in Astronomy*  
1290 *and Space Sciences*, 8, 78
- 1291 Das, A., Sil, M., Gorai, P., Chakrabarti, S. i. K., & Loison, J. C.  
1292 2018, *ApJS*, 237, 9
- 1293 Dickens, J. E., Irvine, W. M., Nummelin, A., et al. 2001,  
1294 *Spectrochimica Acta Part A: Molecular Spectroscopy*, 57, 643
- 1295 Draine, B. T. 1978, *ApJS*, 36, 595
- 1296 Dunning, Thom H., J. 1989, *JChPh*, 90, 1007
- 1297 Endres, C. P., Schlemmer, S., Schilke, P., Stutzki, J., & Müller, H.  
1298 S. P. 2016, *Journal of Molecular Spectroscopy*, 327, 95
- 1299 Etim, E. E., Gorai, P., Das, A., & Arunan, E. 2018, *Ap&SS*, 363, 6
- 1300 Favre, C., Despois, D., Brouillet, N., et al. 2011, *HCOOCH3 as a*  
1301 *probe of temperature and structure of Orion-KL*, , ,  
1302 arXiv:1103.2548
- 1303 Fedoseev, G., Chuang, K.-J., Ioppolo, S., et al. 2017, *The*  
1304 *Astrophysical Journal*, 842, 52
- 1305 Fedoseev, G., Cuppen, H. M., Ioppolo, S., Lamberts, T., &  
1306 Linnartz, H. 2015, *MNRAS*, 448, 1288
- 1307 Fourikis, N., Sinclair, M. W., Robinson, B. J., Godfrey, P. D., &  
1308 Brown, R. D. 1974, *Australian Journal of Physics*, 27, 425
- 1309 Frisch, M. J., Trucks, G. W., Schlegel, H. B., et al. 2013, *Gaussian*  
1310 *09 Revision D.01*, , , gaussian Inc. Wallingford CT
- 1311 Fuchs, G. W., Cuppen, H. M., Ioppolo, S., et al. 2009, *A&A*, 505,  
1312 629
- 1313 Furuya, K., & Persson, M. V. 2018, *MNRAS*, 476, 4994



- 1314 Garrod, R. T., & Herbst, E. 2006, *A&A*, 457, 927
- 1315 Garrod, R. T., & Pauly, T. 2011, *The Astrophysical Journal*, 735, 15
- 1316 Garrod, R. T., Wakelam, V., & Herbst, E. 2007, *A&A*, 467, 1103
- 1317 Garrod, R. T., Weaver, S. L. W., & Herbst, E. 2008, *The*  
1318 *Astrophysical Journal*, 682, 283
- 1319 Gibb, A. G., Wyrowski, F., & Mundy, L. G. 2004, *ApJ*, 616, 301
- 1320 Goldsmith, P. F., & Langer, W. D. 1999, *ApJ*, 517, 209
- 1321 Gorai, P., Bhat, B., Sil, M., et al. 2020, *ApJ*, 895, 86
- 1322 Gorai, P., Das, A., Das, A., et al. 2017a, *ApJ*, 836, 70
- 1323 Gorai, P., Das, A., Majumdar, L., et al. 2017b, *Molecular*  
1324 *Astrophysics*, 6, 36
- 1325 Gorai, P., Das, A., Shimonishi, T., et al. 2021, *ApJ*, 907, 108
- 1326 Gottlieb, C. A. 1973, in *Molecules in the Galactic Environment*,  
1327 ed. M. A. Gordon & L. E. Snyder, 181
- 1328 Goumans, T. P. M. 2011, *MNRAS*, 413, 2615
- 1329 Habing, H. J. 1968, *BAN*, 19, 421
- 1330 Herbst, E., & Leung, C. M. 1986, *ApJ*, 310, 378
- 1331 Hincelin, U., Chang, Q., & Herbst, E. 2015, *A&A*, 574, A24
- 1332 Hiraoka, K., Yamashita, A., Miyagoshi, T., et al. 1998, *The*  
1333 *Astrophysical Journal*, 508, 423
- 1334 Hocuk, S., Szűcs, L., Caselli, P., et al. 2017, *A&A*, 604, A58
- 1335 Hollis, J. M., Jewell, P. R., Lovas, F. J., Remijan, A., & Møllendal,  
1336 H. 2004, *ApJL*, 610, L21
- 1337 Hollis, J. M., Lovas, F. J., Jewell, P. R., & Coudert, L. H. 2002,  
1338 *ApJL*, 571, L59
- 1339 Hunter, E. P. L., & Lias, S. G. 1998, *Journal of Physical and*  
1340 *Chemical Reference Data*, 27, 413
- 1341 Ikeda, M., Ohishi, M., Nummelin, A., et al. 2001, *ApJ*, 560, 792
- 1342 Käser, S., Unke, O. T., & Meuwly, M. 2020, *The Journal of*  
1343 *Chemical Physics*, 152, 214304
- 1344 Keane, J. V., Tielens, A. G. G. M., Boogert, A. C. A., Schutte,  
1345 W. A., & Whittet, D. C. B. 2001, *A&A*, 376, 254
- 1346 Lee, H. H., Herbst, E., Pineau des Forets, G., Roueff, E., & Le  
1347 Bourlot, J. 1996, *A&A*, 311, 690
- 1348 Maury, A. J., Belloche, A., André, P., et al. 2014, *A&A*, 563, L2
- 1349 McElroy, D., Walsh, C., Markwick, A. J., et al. 2013, *A&A*, 550,  
1350 A36
- 1351 McGuire, B. A. 2018, *ApJS*, 239, 17
- 1352 McMullin, J. P., Waters, B., Schiebel, D., Young, W., & Golap, K.  
1353 2007, in *Astronomical Society of the Pacific Conference Series*,  
1354 Vol. 376, *Astronomical Data Analysis Software and Systems*  
1355 XVI, ed. R. A. Shaw, F. Hill, & D. J. Bell, 127
- 1356 Menten, K. M., Walmsley, C. M., Henkel, C., & Wilson, T. L.  
1357 1988, *A&A*, 198, 253
- 1358 Müller, H. S. P., Schlöder, F., Stutzki, J., & Winnewisser, G. 2005,  
1359 *Journal of Molecular Structure*, 742, 215
- 1360 Müller, H. S. P., Thorwirth, S., Roth, D. A., & Winnewisser, G.  
1361 2001, *A&A*, 370, L49
- 1362 Nummelin, A., Dickens, J. E., Bergman, P., et al. 1998, *A&A*, 337,  
1363 275
- 1364 Öberg, K. I., Fuchs, G. W., Awad, Z., et al. 2007, *ApJL*, 662, L23
- 1365 Öberg, K. I., Garrod, R. T., van Dishoeck, E. F., & Linnartz, H.  
1366 2009, *A&A*, 504, 891
- 1367 Olmi, L., Cesaroni, R., & Walmsley, C. M. 1996, *A&A*, 307, 599
- 1368 Pascual-Ahuir, J., Silla, E., Tomasi, J., & Bonaccorsi, R. 1987,  
1369 *Journal of Computational Chemistry*, 8, 778
- 1370 Persson, M. V., Jørgensen, J. K., Müller, H. S. P., et al. 2018, *A&A*,  
1371 610, A54
- 1372 Pickett, H. M., Poynter, R. L., Cohen, E. A., et al. 1998, *JQSRT*,  
1373 60, 883
- 1374 Pizzarello, S., & Weber, A. L. 2004, *Science*, 303, 1151
- 1375 Pontoppidan, K. M., Dartois, E., van Dishoeck, E. F., Thi, W. F., &  
1376 d'Hendecourt, L. 2003, *A&A*, 404, L17
- 1377 Qasim, D., Fedoseev, G., Chuang, K. J., et al. 2019, *A&A*, 627, A1
- 1378 Requena-Torres, M. A., Martín-Pintado, J., Rodríguez-Franco, A.,  
1379 et al. 2006, *A&A*, 455, 971
- 1380 Rimola, A., Taquet, V., Ugliengo, P., Balucani, N., & Ceccarelli, C.  
1381 2014, *A&A*, 572, A70
- 1382 Rivilla, V. M., Beltrán, M. T., Cesaroni, R., et al. 2017, *A&A*, 598,  
1383 A59
- 1384 Rolffs, R., Schilke, P., Zhang, Q., & Zapata, L. 2011, *A&A*, 536,  
1385 A33
- 1386 Sánchez-Monge, Á., Schilke, P., Ginsburg, A., Cesaroni, R., &  
1387 Schmiedeke, A. 2018, *A&A*, 609, A101
- 1388 Sanna, A., Reid, M. J., Menten, K. M., et al. 2014, *The*  
1389 *Astrophysical Journal*, 781, 108
- 1390 Shimonishi, T., Das, A., Sakai, N., et al. 2020, *ApJ*, 891, 164
- 1391 Sil, M., Gorai, P., Das, A., et al. 2018, *ApJ*, 853, 139
- 1392 Sil, M., Gorai, P., Das, A., Sahu, D., & Chakrabarti, S. K. 2017,  
1393 *European Physical Journal D*, 71, 45
- 1394 Sil, M., Srivastav, S., Bhat, B., et al. 2021, arXiv e-prints,  
1395 arXiv:2105.14569
- 1396 Snyder, L. E., Buhl, D., Zuckerman, B., & Palmer, P. 1969,  
1397 *PhRvL*, 22, 679
- 1398 Song, L., & Kästner, J. 2017, *ApJ*, 850, 118
- 1399 Tercero, B., Cernicharo, J., López, A., et al. 2015, *A&A*, 582, L1
- 1400 Tomasi, J., Mennucci, B., & Cammi, R. 2005, *Chemical Reviews*,  
1401 105, 2999, pMID: 16092826
- 1402 Tomasi, J., & Persico, M. 1994, *Chemical Reviews*, 94, 2027
- 1403 Turner, A. M., Koutsogiannis, A. S., Kleimeier, N. F., et al. 2020,  
1404 *ApJ*, 896, 88
- 1405 Turner, B. E. 1977, *ApJL*, 213, L75
- 1406 Turner, B. E., & Apponi, A. J. 2001, *ApJL*, 561, L207
- 1407 Vastel, C., Bottinelli, S., Caux, E., Glorian, J. M., & Boiziot, M.  
1408 2015, in *SF2A-2015: Proceedings of the Annual meeting of the*  
1409 *French Society of Astronomy and Astrophysics*, 313–316
- 1410 Wakelam, V., & Herbst, E. 2008, *ApJ*, 680, 371
- 1411 Wakelam, V., Loison, J. C., Mereau, R., & Ruaud, M. 2017,  
1412 *Molecular Astrophysics*, 6, 22

- 1413 Wakelam, V., Smith, I. W. M., Herbst, E., et al. 2010, *SSRv*, 156,  
1414 13
- 1415 Watanabe, N., & Kouchi, A. 2002, *The Astrophysical Journal*, 571,  
1416 L173
- 1417 Weaver, S. W., Powers, C. R., McCabe, M. N., & Zinga, S. 2018,  
1418 *IAU Symposium*, 332, 305
- 1419 Weber, A. L. 1998, *Origins of Life and Evolution of the Biosphere*,  
1420 28, 259
- 1421 Woods, P. M., Slater, B., Raza, Z., et al. 2013, *ApJ*, 777, 90
- 1422 Woon, D. E. 2002a, *ApJ*, 569, 541
- 1423 —. 2002b, *ApJL*, 571, L177
- 1424 Wyrowski, F., Schilke, P., & Walmsley, C. M. 1999, *A&A*, 341,  
1425 882
- 1426 Zaverkin, V., Lamberts, T., Markmeyer, M. N., & Kästner, J. 2018,  
1427 *A&A*, 617, A25
- 1428 Zuckerman, B., Turner, B. E., Johnson, D. R., et al. 1975, *ApJL*,  
1429 196, L99